http://eprints.gla.ac.uk/137377/

MCNTs@MnO$_2$ Nanocomposite Cathode Integrated with Soluble O$_2$-Carrier Co-salen in Electrolyte for High-Performance Li-Air Batteries

Xiaofei Hu,[†] Jianbin Wang [†] Zifan Li [†] Jiaqi Wang[†] Duncan H. Gregory,[§] and Jun Chen*,[†]

[†]Key Laboratory of Advanced Energy Materials Chemistry (Ministry of Education) and State Key Laboratory of Elemento-Organic Chemistry, Collaborative Innovation Center of Chemical Science and Engineering, College of Chemistry, Nankai University, Tianjin 300071, China

[§]School of Chemistry, University of Glasgow, University Avenue, Glasgow G12 8QQ, UK

ABSTRACT: Li-air batteries (LABs) are promising because of their high energy density. However, LABs are troubled by large electrochemical polarization during discharge and charge, side reactions from both carbon cathode surface/peroxide product and electrolyte/superoxide intermediate, as well as the requirement for pure O$_2$. We here report the solution using multi-wall carbon nanotubes (MCNTs)@MnO$_2$ nanocomposite cathode integrated with N,N'-bis(salicylidene)ethylenediaminocobalt(II) (Co^{II}-salen) in electrolyte for LABs. The advantage of such a combination is that on one hand, the coating layer of δ-MnO$_2$ with about 2-3 nm on MCNTs@MnO$_2$ nanocomposite catalyzes Li$_2$O$_2$ decomposition during charge and suppresses side reactions between product Li$_2$O$_2$ and MCNT surface. On the other hand, Co^{II}-salen works as a mobile O$_2$-carrier and accelerates Li$_2$O$_2$ formation through the reaciton of (Co^{III}-salen)$_2$-O$_2^{2-}$ + 2Li$^+$ + 2e$^-$ → 2Co^{II}-salen + Li$_2$O$_2$. This reaction route overcomes the pure O$_2$ limitation and avoids the formation of aggressive superoxide intermediate (O$_2^-$ or LiO$_2$), which easily attacks organic electrolyte. By using this double-

catalyst system of Co-salen/MCNTs@MnO$_2$, the lifetime of LABs is polonged to 300 cycles at 500 mA g^{-1} (0.15 mA cm^{-2}) with fixed capacity of 1000 mAh g^{-1} (0.30 mAh cm^{-2}) in dry air (21% O$_2$). Furthermore, we up-scale the capacity to 500 mAh (5.2 mAh cm^{-2}) in pouch-type batteries (~4 g, 325 Wh kg^{-1}). This study should pave a new way for the design and construction of practical LABs.

Lithium-air batteries (LABs) have recently attracted extensive academic and technological interest due to their high theoretical energy density of ~3600 Wh kg^{-1} based on the electrochemical reaction pathway of $2Li^+ + O_2 + 2e^- \leftrightarrow Li_2O_2$.[1-5] However, LABs still suffer from three critical issues. The first one is insufficient catalytic activities towards Li$_2$O$_2$ formation/decomposition, leading to large electrochemical polarizition during discharge and charge. The second one is side reactions not only between nonaqueous electrolyte and superoxide intermediate but also between carbon cathode surface and product Li$_2$O$_2$,[6-9] resulting in short cycling life. The third one is slow diffusion and large concentration polarization of oxygen in electrolyte, giving rise to the requirement for high-purity O$_2$. The cathode reactions include the formation of superoxide intermediate (LiO$_2$ or O$_2^-$) and Li$_2$O$_2$ product in discharge and the decomposition of Li$_2$O$_2$ in charge.[10-14] The superoxide intermediate easily decomposes the organic electrolyte; while, the insoluble Li$_2$O$_2$ product that is deposited on carbon cathode tends to oxidize the defects and oxygen-containing radicals on carbon cathode surface. The inexpensive method to increase catalytic activities towards Li$_2$O$_2$ formation/decomposition is worth developing. However, the report on cost-effective methods to prevent carbon cathode surface from side reactions and avoid the formation of superoxide intermediate is still limited.

During reversible cycles of LABs, the Li$_2$O$_2$ formation/decomposition occur at the interface between Li$_2$O$_2$ and cathode surface (or solid catalyst surface), on which the catalytic activity of catalysts and electron conductivity are key factors of the battery performance.[15-17] Cathode

catalysts based on multi-wall carbon nanotubes (MCNTs, >200 S m^{-1}) such as MCNTs@RuO$_2$ are popular, exhibiting advanced performance.[18,19] Replacing noble metal with cheap metal oxides (e.g. MnO$_2$) with controlling the coating thickness to several nanometers is able to lower cost, maintain superior conductivity, and especially avoid side reactions[19-21] between Li$_2$O$_2$ and MCNT surface.

Most of the researches on Li-O$_2$ batteries (LOBs) or LABs are carried out in pure O$_2$ atmosphere to exclude the influence of CO$_2$ and H$_2$O. The O$_2$ partial pressure and O$_2$ solubility in electrolyte solvents have been revealed to play a pivotal role on the battery performance such as discharge capacity and rate capability.[14,22] This will raise a dilemma how LABs perform when they are moved from O$_2$ atmosphere into air or dry air, in which O$_2$ only accounts for 21% versus 78% of N$_2$. Therefore, carriers of high O$_2$ uptake need to be developed for LABs for the sake of the relatively low O$_2$ partial pressure in air. It was found that perfluorotributylamine as a firstly reported O$_2$ carrier was added into the electrolyte to increase the O$_2$ concentration and enhance the discharge capacity and rate capability in pure O$_2$ atmosphere.[23] Even though there are lots of artificial and natural redox mediators for Li-O$_2$ batteries in pure O$_2$,[23-27] no O$_2$ carrier (or shuttle) with both O$_2$-carrier ability and catalytic activity has been investigated in air (21% O$_2$). It is known that N,N'-bis(salicylidene)ethylenediaminocobalt(II) (Co^{II}-salen), one model compound of Schiff base complexes of Co^{II}, can reversibly coordinate and release oxygen in human body,[28-31] suggesting its potential electrochemical application in LABs.[32] Such versatile Co^{II}-salen has not ever been studied in LOBs or LABs, and it has a potential to provide a new reaction route to avoid the formation of superoxide intermediate. Therefore, combining precisely coated nanocomposite of MCNTs@MnO$_2$ and powerful oxygen carrier of Co-salen is of importance to comprehensively enhance the electrochemical performance of LABs in dry air with 21% O$_2$.

We here integrate MCNTs@MnO$_2$ nanocomposite cathode and 5 mM Co^{II}-salen electrolyte for Li-air batteries with 21% O$_2$ condition to obtain high energy density and long cycling life.

MCNTs@MnO$_2$ nanocomposite is synthesized by precisely coating MCNTs by δ-MnO$_2$ layer (2 to 3 nm in thickness), which accelerates Li$_2$O$_2$ decomposition (Li$_2$O$_2$ → O$_2$ + 2Li$^+$ + 2e$^-$) and especially avoids side reactions between Li$_2$O$_2$ and C-O/C-O=C on the surface of MCNTs. Meanwhile, Co^{II}-salen not only works as a carrier of high O$_2$ uptake and thus overcome pure-O$_2$ limitation to LABs, but also realizes the direct generation of Li$_2$O$_2$ via the reaction of (Co^{III}-salen)$_2$-O$_2^{2-}$) + 2Li$^+$ + 2e$^-$ → 2Co^{II}-salen + Li$_2$O$_2$. Importantly, this discharge mechanism avoids the formation of superoxide intermediate and restrains side reactions between superoxide intermediate and electrolyte. The two-catalyst system of Co-salen/MCNTs@MnO$_2$ improves catalytic activity towards Li$_2$O$_2$ formation/decomposition and results in reduced side reactions from electrolyte/superoxide intermediate and carbon cathode surface/product Li$_2$O$_2$. In addition, LABs with Co^{II}-salen based electrolyte in dry air with 21% of O$_2$ plus 78% of N$_2$ can deliver comparable performance to that in pure O$_2$ atmosphere, indicating the advantage of high O$_2$ uptake of the soluble Co^{II}-salen catalyst. This investigation of integrating MCNTs@MnO$_2$ nanocomposite catalyst cathode and soluble O$_2$-carrier of Co-salen electrolyte provides new insights into the design and construction of practical LABs.

MCNTs were coated by δ-MnO$_2$ layer via a room temperature ultrasonic reactioin of $3C + 4MnO_4^- + 4H^+ \rightarrow 3CO_2\uparrow + 4MnO_2 + 2H_2O$. The introduction of δ-MnO$_2$ onto MCNTs is aimed to increase catalytic activity towards Li$_2$O$_2$ decomposition and reduce oxygen-containing radicals (or passivates the defects) on the MCNT surface, inhibiting side reactions of radicals with Li$_2$O$_2$. Figure 1a-c show TEM images of pristine MCNTs, MCNTs@MnO$_2$ (coating time of 60 min), and MCNTs@MnO$_2$-L (coating time of 180 min, L stands for the nanocomposite with larger coating mass of MnO$_2$). The thickness of MnO$_2$ layer of MCNTs@MnO$_2$ is 2 to 3 nm (Figure 1b) and the lattice plane (111) belonging to δ-MnO$_2$ is oberved with interplanar distance of 0.24 nm (inset of Figure 1b). In contrast, MCNTs@MnO$_2$-L depicts nanosheet array of MnO$_2$ on the outer surface of MCNTs (Figure

1c and Supporting Information Figures S1). The existence of δ-MnO$_2$ in MCNTs@MnO$_2$ nanocomposite is also conformed by X-ray photoelectron spectroscopy (XPS, towards Mn2p and Mn3s) and XRD (Supporting Information Figures S2, S3). Soft X-ray absorption spectroscopies (SXAS) suggest that a small amount of low-valence Mn-ion and large amount of Mn (IV) are formed at early stage of the synthesis reaction. As reaction time prolongs, more and more C-O-Mn bonds are formed (Figure 1d-f, detailed description can be seen in the caption of Supporting Information Figures S3). These bonds bridge the coating layer (δ-MnO$_2$) and MCNTs, guaranteeing robust structure stability and fast electron transfer in the nanocomposite. MCNTs@MnO$_2$ has much lower electrochemical impedance (1.26 kΩ) than that of MCNTs@MnO$_2$-L (3.70 kΩ) (Figure 1g), indicating that over loading of MnO$_2$ on MCNTs reduces the electro-conductivity of the final nanocomposite.
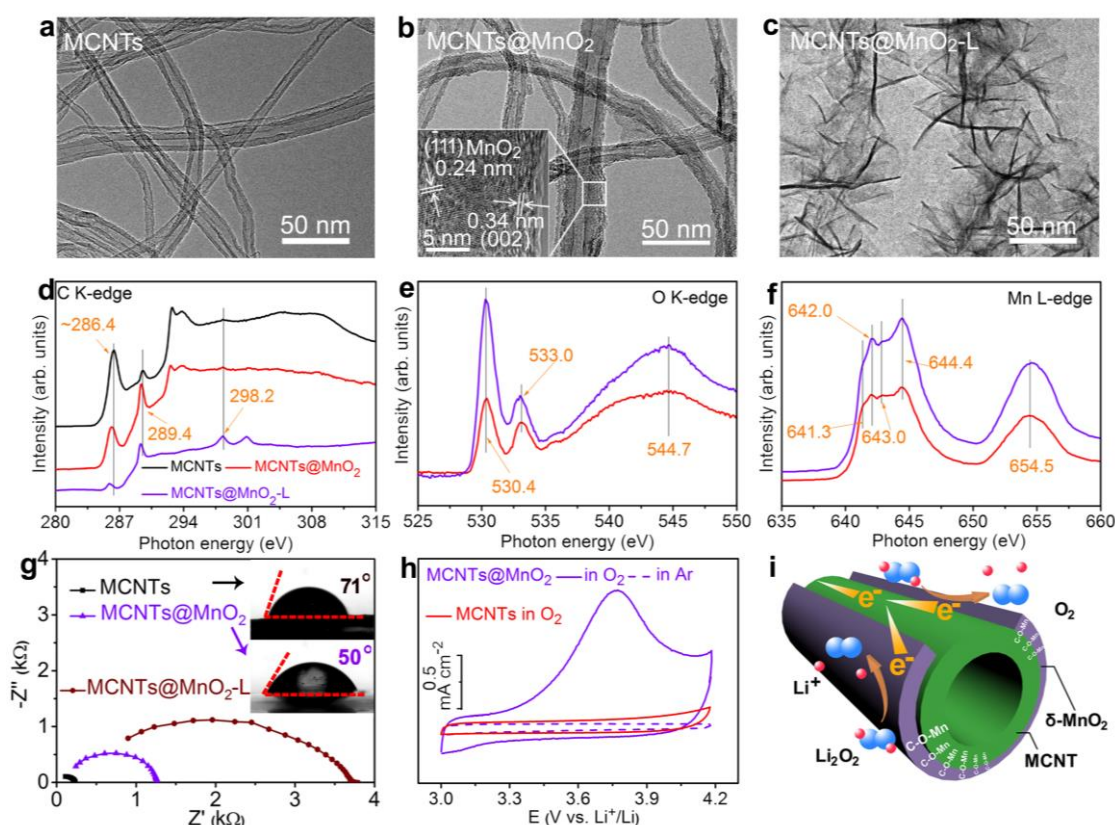

Figure 1. Synthesis and analysis of MCNTs@MnO$_2$. (a to c) TEM images of (a) pristine MCNTs, (b) MCNTs@MnO$_2$, and (c) MCNTs@MnO$_2$-L. The inset of (b) is a HRTEM image of MCNTs@MnO$_2$. (d to f) Soft X-ray absorption spectroscopies of (d) C K-edge, (e) O K-

edge, and (f) Mn L-edge. (g) Powder electrochemical impedance spectroscopy (PEIS) of MCNTs, MCNTs@MnO$_2$, and MCNTs@MnO$_2$-L. The inset is contact angles of MCNTs and MCNTs@MnO$_2$. (h) CV curves with speed of 1 mV s^{-1} after discharging to 1000 mAh g^{-1}. (i) Schematic diagram of Li$_2$O$_2$ decomposition on MCNTs@MnO$_2$.

The MCNT radicals including C-O, O-C=O, and C=O groups are reactive to Li$_2$O$_2$/O$_2^-$ and successfully coated by MnO$_2$, which is indicated by FTIR (Supporting Information Figure S4a) and XPS towards C1s and O1s (Supporting Information Figure S4b,c). The coating MnO$_2$ layer is further verified by pore-size distribution analysis of MCNTs and MCNTs@MnO$_2$, demonstrating fewer tiny holes (2 to 3 nm) on the nanocomposite surface (Supporting Information Figures S5). Thermo-gravimetric analysis together with energy dispersive spectrometer reveals that the mass content of MnO$_2$ in the composite is about 57.0 wt% (Supporting Information Figures S6). This MnO$_2$ coating layer prevents the unwanted decomposition of both the MCNT surface and the ether (tetraglyme) solvent, which is a trouble for LABs.[33] Meanwhile, the contact angle of the nanocomposite towards tetraethylene glycol dimethyl ether (TEGDME) is 50 º, which is 21 º smaller (inset of Figure 1g) than that of naked MCNTs (71 º), suggesting that the wettability of the nanocomposite towards TEGDME-based electrolyte is increased by the coating layer of MnO$_2$.

To confirm the catalytic activity towards Li$_2$O$_2$ decomposition of MCNTs@MnO$_2$ refering to MCNTs, CV between 3.0 and 4.2 V under O$_2$ or Ar was conducted in coin-type batteries (Figure 1h and Supporting Information Figures S7). In the anodic process, the oxidation of Li$_2$O$_2$ begins at 3.30 V with the aid of MCNTs@MnO$_2$. This oxidation onset potential is much lower than that of MCNTs, which exhibits only a weak oxidation peak. The enhanced performance towards Li$_2$O$_2$ decomposition obviously results from the MnO$_2$ layer of MCNTs@MnO$_2$. Notably, there is no oxidation peak of CV in Ar with the aid of MCNTs@MnO$_2$, eliminating the possiblility that the oxidation peak is related to

6

pseudocapacitance of the MnO_2. We use a cartoon to simply describe the catalysis processes of $MCNTs@MnO_2$ nanocomposite (Figure 1i). First, by forming C-O-Mn bond, MCNTs modify the Mn-O bond and the surface configuration of MnO_2, which accelerates Li_2O_2 decomposition ($Li_2O_2 \rightarrow O_2 + 2Li^+ + 2e^-$). Second, the intact inner walls of MCNTs guarantee fast charge transfer.
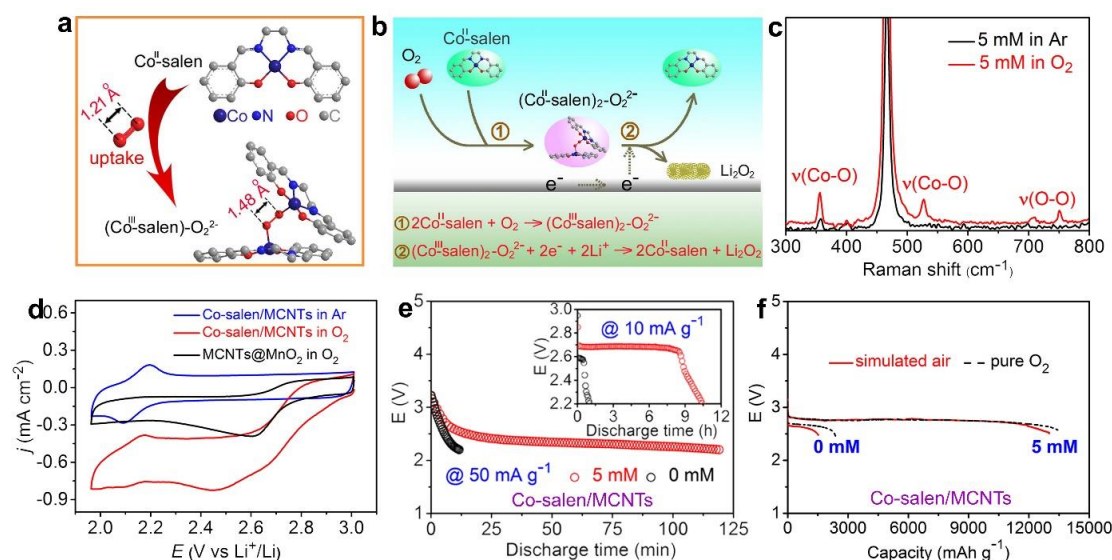

Figure 2. Soluble catalyst analysis of Co-salen for Li_2O_2 formation. (a) Molecular structure of Co^{II}-salen and its optimized structure after O_2 uptake, H atoms are omitted for clarity. (b) Schematic diagram and reaction mechanism of the LABs with Co^{II}-salen in the electrolyte during discharge and charge. (c) Raman spectra of Co^{II}-salen powders in Ar and O_2. This test does not involve LiTFSI/TEGDME electrolyte. (d) CV curves of ORR. Rate: 10 mV s^{-1}. (e) Discharge curves of the LABs with and without 5 mM Co^{II}-salen in the electrolyte after successive rest in O_2 and Ar at 10 mA g^{-1} (3 μA cm^{-2}) and 50 mA g^{-1} (15 μA cm^{-2}). (f) Discharge profiles at 500 mA g^{-1} in O_2 or simulated air with 21% O_2.

The functions of Co^{II}-salen in LABs are individually investigated on MCNT cathode (Figure 2a and b). In dry air, each two units of Co^{II}-salen can coordinate with one unit of O_2 to form $(Co^{III}$-salen$)_2$-O_2^{2-}, which has been confirmed by electronic spectra[31] and density

functional theory (DFT) calculation (Supporting Information Scheme S1, Table S1 and S2). The O_2 in the adduct is activated by showing the O-O bond length of 1.48 Å, longer than its original 1.21 Å (Figure 2a). It is close to the O-O bond length of O_2^{2-}, 1.55 Å, in Li_2O_2 and Na_2O_2.[34] In the discharging process, the $(Co^{III}\text{-salen})_2\text{-}O_2^{2-}$ combines with Li^+ ions and gets reduced on the cathode to regenerate Co^{II}-salen and produce Li_2O_2 deposits both in solution phase and on cathode surface (Figure 2b). Thus, this reaction mechanism benefits high capacity and normal operation in low oxygen partial pressure. Importantly, it also avoids the intermediate formation of superoxide and thus reduces the oxidation of organic electrolyte. The Co^{II}-salen can work repeatedly to increase the O_2 concentration in the electrolyte and promote the Li_2O_2 formation. This will be evidenced by the discharge/charge profiles and the XRD patterns later. The Co^{II}-salen after exposed to O_2 for 2 hours presents three characteristic stretching vibration peaks as indicated in Raman spectra in Figure 2c, as well as the Co^{II}-salen in Ar. The two at 360 and 526 cm^{-1} and the one at 752 cm^{-1} are assigned to $\nu_{(Co\text{-}O)}$ and $\nu_{(O\text{-}O)}$, respectively.[35] This suggests the interaction and electron transfer between Co^{II}-salen and O_2 molecules and facile O_2 uptake by Co^{II}-salen. According to above DFT calculation and Raman test, coordination of $[(Co^{II}\text{-salen})_2\text{-}O_2]$ leads to the electron shift from Co^{II} to O_2. This makes O_2 reduced to form O_2^{2-}. Simultaneously, Co^{II} is oxidized closely to Co^{III}. Thus, we describe the coordinated adduct as $(Co^{III}\text{-salen})_2\text{-}O_2^{2-}$.

By comparing the oxygen reduction reaction (ORR) onset potential and current density in linear sweep voltammetry (LSV), the optimal concentration of Co-salen in 1 M LiTFSI/TEGDME is 5 mM (Supporting Information Figure S8). The LABs with different catalytic systems, i.e. $MCNTs@MnO_2$ cathode without Co^{II}-salen in the electrolyte and MCNT cathode with 5 mM Co^{II}-salen in the electrolyte, present different redox peaks under O_2 and Ar atmosphere as shown in the cyclic voltammetry curves (CVs) of Figure 2d. In the cathodic process, there exists two reduction peaks at 2.7 and 2.1 V for LABs with Co^{II}-salen in O_2. The former one is ascribed to the promoted ORR by the adduct $(Co^{III}\text{-salen})_2\text{-}O_2^{2-}$ as

8

described by the DFT calculation and Raman spectra in Figure 2a-c. The latter one is due to the redox couple of Co^{II}/Co^{I} in Co^{II}-salen, which shows larger reduction currents than that in Ar but actually does not take part in ORR process. In contrast, the LABs without Co^{II}-salen in O_2 present one ORR peak at 2.3 V, which is negatively shifted by 300 mV than that with 5 mM Co^{II}-salen in O_2. This demonstrates the largely accelerated ORR process of O_2/Li_2O_2 by Co^{II}-salen in the electrolyte.

After the rest in O_2 for 20 hours of LABs with and without 5 mM Co^{II}-salen in electrolyte, the O_2 atmosphere is switched to Ar. Then, LABs begin to discharge as displayed in Figure 2e. This "air-switch step" makes it certain that all the oxygen used during discharging process comes from dissolved oxygen in electrolyte and would not be replenished from the atmosphere. The discharge time of LABs with Co^{II}-salen is almost 10 times of that without Co^{II}-salen at both 10 mA g^{-1} (3 µA cm^{-2}) and 50 mA g^{-1} (15 µA cm^{-2}). The selection of small discharge current aims to reduce the effect of O_2-concentration polarization on O_2-comsumption calculation. According to discharge capacity, the apparent O_2 solubility of electrolyte with 5 and 0 mM salen is 4.61 mM and 0.49 mM, respectively (the caculation process can be seen in Supporting Information). Generally speaking, the capacity is limited by many factors such as the pore volume, surface area of the cathode, and surface passivation of active sites, as discharge proceeds. While, the total discharge capacity used to calculate O_2 solubility is 0.032 mAh cm^{-2}, which is only 0.59% limitation of the discharge capacity (>5.4 mAh cm^{-2}) of the cathode (this maximum will be discussed later). There is still a mass of residual pore volume and surface area for Li_2O_2 deposition. Therefore, the effect of the above factors on discharge capacity used to calculate O_2 solubility is negligible. When fixing the reduction potential of 2.5 V vs. Li^+/Li on glass carbon electrodes, the oxygen reduction current of Co-salen is also much larger than that without Co-salen (Supporting Information Figure S9). This implies the much improved catalytic activity of Co-salen and its high reversible O_2 uptake capability. In order to evaluate the feasibility of Co^{II}-salen in LABs, dry

air (21% O_2) without H_2O is employed. As shown in Figure 2f, LABs with 5 mM Co^{II}-salen operated in dry air can deliver a large capacity of ~13050 mAh g^{-1} (3.9 mAh cm^{-2}), which is close to that in pure O_2. However, without the addition of Co^{II}-salen in the electrolyte, the discharge capacities of the LABs are reduced to 1522 mAh g^{-1} (0.46 mAh cm^{-2}) in dry air and 2370 mAh g^{-1} (0.71 mAh cm^{-2}) in pure O_2. This suggests that the Co^{II}-salen can effectively transport O_2 from dry air into the electrolyte, compensating the low O_2 partial pressure in dry air. When it comes to charging, Co-salen and its sisters, namely Ni-salen and Fe-salen, do not show superiority compared with their absence (Supporting Information Figures S10 and S11). Therefore, the O_2-carrier of Co-salen really needs MCNTs@MnO_2 nanocomposite to construct two-catalyst system of Co-salen/MCNTs@MnO_2 for suppressing side reactions, overcoming pure O_2 limitation, and promoting Li_2O_2 formation/decomposition in LABs.
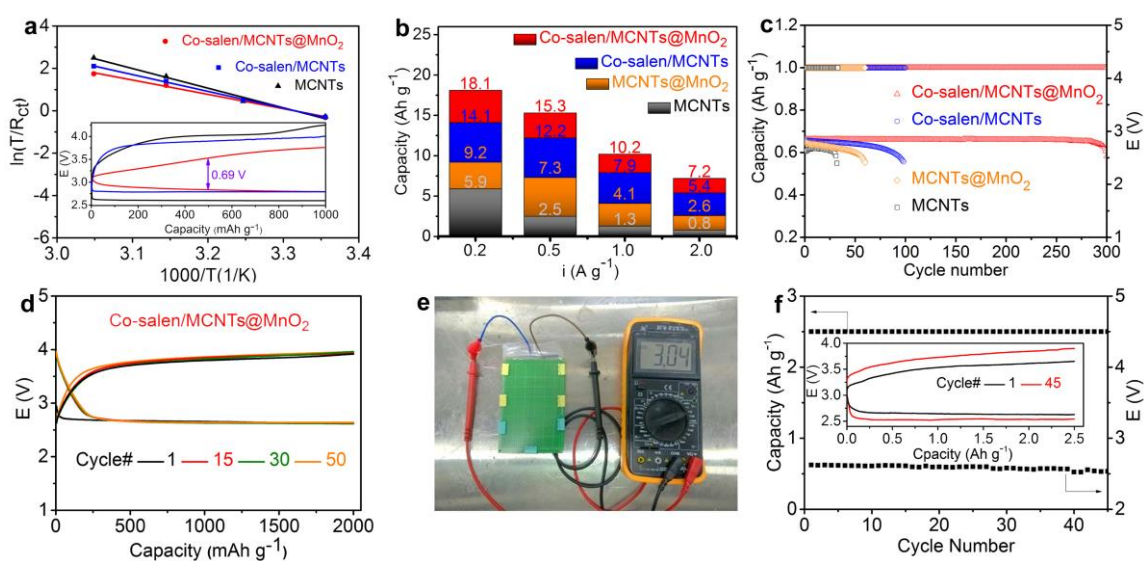

Figure 3. Batteries performance in dry air (21% O_2). (a) Apparent activation energy calculation. The fitting curves present the relationship between $\ln(T/R_{ct})$ and 1000/T. The inset graph is comparison of operating overpotentials at 100 mA g^{-1} (0.03 mA cm^{-2}). (b) Rate capability comparison. (c) Cyclability comparison with controlled capacity of 1000 mAh g^{-1} (0.30 mAh cm^{-2}) at 500 mA g^{-1} (0.15 mA cm^{-2}). (d) Discharge/charge profiles at 500 mA g^{-1} with cut-off capacity of 2000 mAh g^{-1} (0.60 mAh cm^{-2}). (e) A photograph of prototype LABs.

(f) Cyclability and inset discharge/charge curves of the prototype LABs at 100 mA g^{-1} with capacity of 2500 mA g^{-1} (100 mAh) based on the mass of cathode catalyst.

We assembled CR2032 coin-type LABs using different catalytic systems, namely, MCNTs, Co-salen/MCNTs, MCNTs@MnO$_2$, and two-catalyst system of Co-salen/MCNTs@MnO$_2$. In comparison with the discharge/charge overpotential (1.42 V) of MCNTs-based cathode and Co-salen/MCNTs, the two-catalyst system of Co-salen/MCNTs@MnO$_2$ exhibits reduced overpotential gap of 0.69 V during the initial cycle at 100 mA g^{-1} (0.03 mA cm^{-2}) (inset of Figure 3a). The sharp reduction of potential gap indicates the superior ORR and oxygen evolution reaction (OER) activity of Co-salen/MCNTs@MnO$_2$, which is also confirmed by activation energy caculation (Figure 3a). The corresponding values of LABs with MCNTs, Co-salen/MCNTs, and Co-salen/MCNTs@MnO$_2$ are 77.1, 65.6, and 56.2 kJ mol^{-1}, respectively, revealing both ORR and OER catalytic superiority of the two-catalyst system with Co-salen/MCNTs@MnO$_2$.

With the increase of the current densities, the two-catalyst system always has 3 to 9 times larger discharge capacity than that of MCNTs (Figure 3b). For example, the two-catalyst system displays 18100 mAh g^{-1} (5.4 mAh cm^{-2}) at 200 mA g^{-1} (0.06 mA cm^{-2}). While the battery with MCNTs just performs 5900 mAh g^{-1} (1.8 mAh cm^{-2}). Even at the highest current density of 2000 mA g^{-1} (0.60 mA cm^{-2}), LABs with two-catalyst system still display a discharge capacity of 7200 mAh g^{-1} (2.2 mAh cm^{-2}). In contrast, LABs with MCNTs just show 800 mAh g^{-1} (0.24 mAh cm^{-2}). Notably, LABs with Co-salen/MCNTs depict ~80% capacity of two-catalyst system, indicating that Co-salen makes the main contribution to the discharge capacity. The LABs with two-catalyst system present stable discharge terminal voltage around 2.80 V during 300 cycles (Figure 3c). While, LABs with Co-salen/MCNTs and MCNTs only run for 98 and 30 cycles, respectively, both of which are much shorter than that of two-catalyst system, demonstrating the vitally important role of MnO$_2$ layer on

rechargeability. In addition, LABs with MCNTs@MnO_2 run for 30 more cycles than that of MCNTs, revealing the positive effect of the MnO_2 layer on the stability of the MCNTs. The prolonged lifetime of LABs with two-catalyst system results from high catalytic activities and effective suppression of side reactions. With the increase of the current density to 1000 mA g^{-1} (0.3 mA cm^{-2}) and 2000 mA g^{-1} (0.6 mA cm^{-2}) (Supporting Information Figure S12), the LABs using two-catalyst system present flat discharge plateaus and charge potentials below 4.5 V, which are comparable to that at a smaller current density of 250 mA g^{-1} (0.075 mA cm^{-2}) with only MCNTs.

Furthermore, LABs with extended capacity of 2000 mAh g^{-1} (0.6 mAh cm^{-2}) still keep rechargeable for 50 cycles (Figure 3d) without fading. When we extend the mass loading from 0.3 mg cm^{-2} to 1.0 mg cm^{-2}, LABs with two-catalyst system show that the overpotential gap at 100 mA g^{-1} (0.1 mA cm^{-2}) is increased from 0.69 V to 0.85 V and stably runs for 200 cycles with fixed capacity of 1000 mAh g^{-1} (1.0 mAh cm^{-2}) at 500 mA g^{-1} (0.5 mA cm^{-2}). In the conditions of using both low and high loading mass, LABs with two-catalyst system always perform better than that with MCNTs in terms of overpotentials and cyclability (Supporting Information Figure S13). The discharge capacity of LABs with Co-salen/MCNTs in Ar is negligible when the discharge terminal voltage is limited to 2.5 V (Supporting Information Figure S14), indicating that the discharge capacity in dry air only comes from oxygen-involved electrochemical reaction. The superior rate performance and cycling stability of the LABs with two-catalyst system in dry air are attributed to the fast transport and facile uptake of O_2 and the bifunctional catalytic activity of Co^{II}-salen/MCNTs@MnO_2 system.

Because high-capacity and high-energy density are highly needed for practical applications, we further assemble large-scale batteries (12 cm × 8 cm) (Figure 3e and Supporting Information Figure S15). Reversible capacity of 500 mAh (5.2 mAh cm^{-2}) at 5 mA (0.052 mA cm^{-2}) is obtained (Supporting Information Figure S16). Based on the total mass of the

battery (4.0 g), the energy density is 325 Wh kg^{-1}, which is higher than that of commercial Li-ion batteries (~200 Wh kg^{-1}).[36] This means the potential application of LABs with two-catalyst system in air. At the depth of 20% discharge/charge (2500 mAh g^{-1}, 1.0 mAh cm^{-2}), the capacity retention of LABs is near 100% after 45 cycles and the retention of discharge terminal is 96.8% (Figure 3f).

The superior rechargeability of LABs with two-catalyst system of Co-salen/MCNTs@MnO$_2$ is also verified by reversible formation and decomposition of discharge product Li$_2$O$_2$ (Supporting Information Figure S17). Quantitative detection of O$_2$ during battery charging shows a much higher OER efficiency of two-catalyst system than that with only MCNTs (Supporting Information Figure S18). Moreover, the obvious difference in chemical yield of Li$_2$O$_2$ between two-catalyst system and its counter part further shows an effective suppression of side reactions because of Co-salen/MCNTs@MnO$_2$ (Supporting Information Figure S19).

In conclusion, we integrate nanocomposite catalyst of MCNTs@MnO$_2$ cathode and soluble O$_2$-carrier of Co-salen in electrolyte for LABs to operate in dry air with only 21% of O$_2$. The δ-MnO$_2$ coating layer (2 to 3 nm) on MCNTs@MnO$_2$ nanocomposite catalyzes Li$_2$O$_2$ decomposition on charge and suppresses side reactions between MCNT surface and Li$_2$O$_2$. Meanwhile, the facile and large O$_2$ uptake capability of Co-salen enables LABs to deliver a large discharge capacity of 13050 mAh g^{-1} (3.9 mAh cm^{-2}), comparable to that in pure O$_2$ atmosphere. The Co-salen coordinates with O$_2$ to form (Co^{III}-salen)$_2$-O$_2$$^{2-}$, which avoids the formation of superoxide intermediate (O$_2$$^{-}$ or LiO$_2$) and thus reduces the oxidation of electrolyte. Furthermore, the formation of Li$_2$O$_2$ is also catalyzed by Co-salen. With the two-catalyst system of Co-salen/MCNTs@MnO$_2$, LABs present discharge terminal voltage of ~2.80 V for 300 cycles due to effective catalytic activities and successful suppression of side reactions. Prototype LABs are constructed to demonstrate an energy density of 325 Wh kg^{-1}.

This study should pave a new way for the design and construction of LABs with high-energy density and long cycling.

ASSOCIATED CONTENT

Supporting Information

Details of the synthesis, characterization and electrochemical measurements can be found in the Supporting Information. This material is available free of charge via the Internet at http://pubs.acs.org.

AUTHOR INFORMATION

Corresponding Author

*E-mail: chenabc@nankai.edu.cn

Notes

The authors declare no competing financial interest.

REFERENCES

(1) Abraham, K. M.; Jiang, Z. *J. Electrochem. Soc.* **1996**, *143*, 1–5.

(2) Peng, Z.; Freunberger, S. A.; Chen, Y.; Bruce, P. G. *Science* **2012**, *337*, 563–566.

(3) Cheng, F. Y.; Chen, J. *Chem. Soc. Rev.* **2012**, *41*, 2172–2192.

(4) Harding, J. R.; Lu, Y.; Tsukada, Y.; Shao-Horn, Y. *Phys. Chem. Chem. Phys.* **2012**, *14*, 10540–10546.

(5) Zhang, K.; Han, X. P.; Hu, Z.; Zhang, X. L.; Tao, Z. L.; Chen, J. *Chem. Soc. Rev.* **2015**, *44*, 699–728.

(6) Luntz, A. C.; McCloskey, B. D. *Chem. Rev.* **2014**, *114*, 11721–11750.

(7) Lu, J.; Li, L.; Park, J.-B.; Sun, Y.-K.; Wu, F.; Amine, K. *Chem. Rev*. **2014**, *114*, 5611–5640.

(8) Li, L. J.; Liu, C.; He. G.; Fan, D. L.; Manthiram, A. *Energy Environ. Sci.* **2015**, *8*, 3274–3282.

(9) Kwak, W.; Lau, K. C.; Shin, C.-D.; Amine, K.; Curtiss, L. A.; Sun, Y.-K. *ACS Nano* **2015**, *9*, 4129–4137.

(10) Oh, S. H.; Black, R.; Pomerantseva, E.; Lee, J.-H.; Nazar, L. F. *Nature Chem*. **2012**, *4*, 1004–1010.

(11) Hu, Y.; Zhang, T.; Cheng, F.; Zhao, Q.; Han, X.; Chen, J. *Angew. Chem. Int. Ed.* **2015**, *54*, 4338–4343.

(12) Hu, X.; Cheng, F.; Han, X.; Zhang, T.; Chen, J. *Small* **2015**, *11*, 809–813.

(13) Cheng, F.; Shen, J.; Peng, B.; Pan, Y.; Tao, Z.; Chen, J. *Nature Chem*. **2011**, *3*, 79–84.

(14) Landa-Medrano, I.; Pinedo, R.; de Larramendi, I. R.; Ortiz-Vitoriano, N.; Rojo, T. *J. Electrochem. Soc*. **2015**, *162*, A3126–A3132.

(15) Liang, Y.; Wang, H.; Diao, P.; Chang, W.; Hong, G.; Li, Y.; Gong, M.; Xie, L.; Zhou, J.; Wang, J.; Regier, T. Z.; Wei, F.; Dai, H. *J. Am. Chem. Soc.* **2012**, *134*, 15849−15857.

(16) Zhong, L.; Mitchell, R. R.; Liu, Y.; Gallant, B. M.; Thompson, C. V.; Huang, J. Y.; Mao, S. X.; Shao-Horn, Y. *Nano Lett.* **2013**, *13*, 2209–2214.

(17) Kushima, A.; Koido, T.; Fujiwara, Y.; Kuriyama, N.; Kusumi, N.; Li, J. *Nano Lett.* **2015**, *15*, 8260–8265.

(18)   Yilmaz, E.; Yogi, C.; Yamanaka, K.; Ohta, T.; Byon, H. R. *Nano Lett.* **2013**, *13*, 4679−4684.

(19)   Jian, Z. L.; Liu, P.; Li, F. J.; He, P.; Guo, X. W.; Chen, M. W.; Zhou, H. S. *Angew. Chem. Int. Ed.* **2014**, *53*, 442–446.

(20)   Xu, J.-J.; Chang, Z.-W.; Wang, Y.; Liu, D.-P.; Zhang, Y.; Zhang, X.-B. *Adv. Mater.* **2016**, DOI: 10.1002/adma.201603454.

(21)   Hu, X. F.; Cheng, F. Y.; Zhang, N.; Han, X. P.; Chen, J. *Small* **2015**, *11*, 5545–5550.

(22)   Yang, X.; Xia, Y. *J. Solid State Electrochem.* **2010**, *14*, 109–114.

(23)   Wang, Y.; Zheng, D.; Yang, X.-Q.; Qu, D. *Energy Environ. Sci.* **2011**, *4*, 3697–3702.

(24)   Chen, Y.; Freunberger, S. A.; Peng, Z.; Fontaine, O.; Bruce, P. G. *Nature Chem.* **2013**, *5*, 489–494.

(25)   Lacey, M. J.; Frith, J. T.; Owen, J. R. *Electrochem. Commun.* **2013**, *26*, 74–76.

(26)   Bergner, B. J.; Schürmann, A.; Peppler, K.; Garsuch, A.; Janek, J. *J. Am. Chem. Soc.* **2014**, *136*, 15054–15064.

(27)   Ryu, W.-H.; Gittleson, F. S.; Thomsen, J. M.; Li, J. Y.; Schwab, M. J.; Brudvig, G. W.; Taylor, A. D. *Nature Commun.* **2016**, *7*, 12925–12934.

(28)   Appleton, T. G. *J. Chem. Edu.* **1977**, *54*, 443–444.

(29)   Bailes, R. H.; M. Calvin, *J. Am. Chem. Soc.* **1947**, *69*, 1886–1893.

(30)   Burness, J. H.; Dillard, J. G.; Taylor, L. T. *J. Am. Chem. Soc.* **1975**, *97*, 6080–6088.

(31)   Lever, A. B. P.; Gray, H. B. *J. Am. Chem. Soc.* **1978**, *11*, 348–355.

(32)   Buriez, O.; Moretto, L. M.; Ugo, P. *Electrochim. Acta* **2006**, *52*, 958–964.

(33)   Xie, J.; Yao, X.; Chen, Q.; Madden, I. P.; Dornath, P.; Chang, C.-C.; Fan, W.; Wang, D. *Angew. Chem. Int. Ed.* **2015**, *54*, 4299–4303.

(34)   Wang, Z.; Sun, J.; Cheng, Y.; Niu, C. *J. Phys. Chem. Lett.* **2014**, *5*, 3919–3923.

(35)   Suzuki, M.; Ishiguro, T.; Kozuka, M.; Nakamoto, K. *Inorg. Chem.* **1981**, *20*, 1993–1996.

(36)   Dunn, B.; Kamath, H.; Tarascon, J. M. *Science* **2011**, *334*, 928–935.

TOC
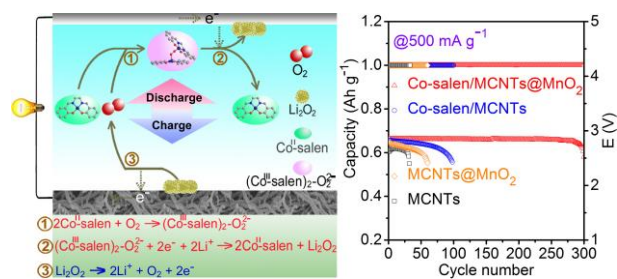
Supporting Information

MCNTs@MnO$_2$ Nanocomposite Cathode Integrated with Soluble

O$_2$-Carrier Co-salen in Electrolyte for High-Performance Li-Air Batteries

Xiaofei Hu,[†] Jianbin Wang,[†] Zifan Li,[†] Jiaqi Wang,[†] Duncan H. Gregory,[§] and Jun Chen*,[†]

[†]Key Laboratory of Advanced Energy Materials Chemistry (Ministry of Education) and State Key Laboratory of Elemento-Organic Chemistry, Collaborative Innovation Center of Chemical Science and Engineering, College of Chemistry, Nankai University, Tianjin 300071, China

[§]School of Chemistry, University of Glasgow, University Avenue, Glasgow G12 8QQ, UK.

Corresponding Author
*E-mail: chenabc@nankai.edu.cn

Contents:

1. **Preparation of the electrolyte.**

2. **Synthesis of MCNTs@MnO$_2$.**

3. **Materials characterization.**

4. **Electrochemical tests.**

5. **Assembly of pouch-type LABs.**

6. **Rotating-Disk-Electrode (RDE) measurements.**

7. **Powder electrochemical impedance spectroscopy (PEIS) measurements.**

8. **O$_2$ solubility calculation.**

9. **Figure S1. The morphology and crystal lattice of MCNTs@MnO$_2$-L.**

10. **Figure S2. XPS survey of MCNTs@MnO$_2$**

11. **Figure S3. XRD of MCNTs@MnO$_2$ and MCNTs@MnO$_2$-L.**

12. **Figure S4. FT-IR and XPS of MCNTs and MCNTs@MnO2 nanocomposite.**

13. **Figure S5. Pore distribution of MCNTs and MCNTs@MnO$_2$.**

14. **Figure S6. Thermal gravity analysis (TGA) curves and EDS spectra of MCNTs@MnO$_2$.**

15. **Figure S7. CV curves with speed of 1 mV s^{-1}.**

16. **Figure S8. LSV curves in electrolytes with different concentrations of CoII-salen on glassy carbon RDE.**

17. **Figure S9. Current-time curves with 0 mM or 5 mM Co^{II}-salen on MCNTs coated glassy carbon electrode at 400 r min^{-1}.**

18. **Figure S10. Discharge/charge profiles of LABs with and without Co^{II}-salen in electrolytes in dry air.**

19. **Figure S11. Electrochemical performance of LABs with 5 mM Fe^{II}-salen and 5 mM Ni^{II}-salen in electrolytes.**

20. **Figure S12. Charge/discharge curves of MCNTs@MnO$_2$ based Li–air batteries at different current densities.**

21. **Figure S13. Battery performance in dry air with loading mass of 1 mg cm^{-2}.**

22. **Figure S14. Discharge curve of LABs with 5 mM Co-salen and MCNT cathode in Ar.**

23. **Figure S15.The assembly process of pouch-type LABs.**

24. **Figure S16. Discharge/charge profiles of pouch-type batteries at 100 mA g^{-1}.**

25. **Figure S17. Process analysis of LABs with Co-salen/MCNTs@MnO$_2$ or only MCNTs..**

Preparation of the electrolyte

Tetraethylene glycol dimethyl ether (TEGDME) was purchased from Sigma-Aldrich and dried over 4 Å molecular sieves. Lithium bis(trifluoromethanesulfonyl)imide (LiTFSI) was used as received from J&K Chemical. Co^{II}-salen was from Sigma-Aldrich. The electrolyte was prepared by mixing the solvent, LiTFSI, and Co^{II}-salen in the Ar-filled glovebox (Mikrouna Universal 2440/750). The concentration of LiTFSI in TEGDME was 1 mol L^{-1}. The Co^{II}-salen in TEGDME was controlled from 1 to 5 and 20 mmol L^{-1}.

Synthesis of MCNTs@MnO$_2$

The composite of multi-wall CNT@MnO$_2$ (MCNTs@MnO$_2$) was synthesized via two-step sonication. For step 1, commercial multi-wall CNTs (5.5 mg, Beijing Cnano Technology Limited) were added to the aqueous solution of 1.84 M H_2SO_4 (11 ml) and sonicated for 60 min at room temperature (~20 °C) in a plastic tube. For step 2, after we suction out acid liquor of 8 ml from the tube and add aqueous solution of 0.1 M $KMnO_4$ (8 ml) back, the original tube was sonicated for 60 min at room temperature (~20 °C). The preparation process is easily scaled by increasing the number of plastic tube. Once done, the contents was centrifuged with and DI water (deionized water) and absolute ethyl alcohol several times. Finally, the obtained products was dried at 100 °C overnight in ambient air. MCNTs@MnO$_2$-L was synthesized sonication for 180 min in step 2, and the other conditions are the same as MCNTs@MnO$_2$.

Materials characterization

The composites of MCNT, MCNTs@MnO$_2$, MCNTs@MnO$_2$-L, and discharge product in Li–air batteries were characterized by powder X-ray diffraction (Rigaku MiniFlex600, Cu Kα radiation). The content of C in MWCNT@MnO$_2$ was calculated by Thermogravimetric analysis (TGA) with a heating rate 5 °C min^{-1} from 20 °C to 760 °C in air atmosphere. The Brunauer-Emmett-Teller (BET) specific surface area was obtained by the N$_2$ adsorption–desorption isotherm at 77 K (BELSORP-mini instrument). Raman spectra of Co^{II}-salen with and without exposure to O$_2$ were collected on DXR, Thermo Fisher Scientific with excitation at 532 nm from an Ar-ion laser. The discharge products of LABs were characterized by powder X-ray diffraction (Rigaku MiniFlex600, Cu Kα radiation). The morphologies of the products were observed by field-emission scanning electron microscopy (SEM, JEOL JSM7500F) and transmission electron microscopy (TEM, Tecnai G2 F20).

Electrochemical tests

The Electrochemical performance of nonaqueous Li–air was tested at room temperature using CR2032 coin-type batteries. These batteries consist of a lithium foil anode, a glass fiber separator (16 mm in diameter, 0.3 mm in thickness, porosity 92%–98%), and an air electrode. The cathode is one piece of Ni foam evenly coated by 90 wt% catalyst (MCNTs, MCNTs@MnO$_2$, or MCNTs@MnO$_2$-L) and 10 wt% polyvinylidene fluoride (PVdF). The electrolyte is 100 μl of 1 M LiTFSI (lithium bis-(trifluoromethanesulfonyl)-imide) in TEGDME (tetraethylene glycol dimethyl ether) with or without Co^{II}-salen. For cathodes, the total mass loading on the Ni foam

is 0.3 and 1.0 mg cm^{-2} (the mass of each piece of Ni foam is about 22.6 mg). The battery capacity in this study is based on the mass of MCNTs or MCNTs@MnO$_2$ nanocomposite on cathode. Towards the same dischrge capacity, e.g. 0.3 mAh cm^{-2}, the mass of Li$_2$O$_2$ on cathodes is 0.26 mg cm^{-2}. All the batteries were assembled in a glove box (Mikrouna Universal 2440/750) with H$_2$O and oxygen content < 2 ppm. The gas for battery operation is high-pure oxygen or dry air that is composed of 21 % of O$_2$ and 78% of N$_2$. After resting for 10 to 20 h, the batteries were subjected to galvanostatic discharge/charge on a LAND battery testing system at room temperature.

Assembly of pouch-type LABs

Pouch-type LABs are assembled and investigated. They are made up of two porous fixture boards (8.0 × 12.0 cm^2), a plastic bag (8.0 × 13.0 cm^2, 0.30 g), a Li foil anode (7.5 × 10 cm^2, 0.28 g), a glass fiber separator (7.8 × 11.1 cm^2) containing electrolyte of 1 M LiTFSI/TEGDME and 5 mM Co-salen (2.00 g), and a carbon paper cathode (7.6 × 10.9 cm^2, 0.30 g) with 40 mg MCNTs@MnO$_2$. The total mass of pouch-type LABs is ~4.0 g except for the mass of electric wires and fixture boards. It is worth noting that one side of each plastic bag is punched with many pores for air transfer.

Rotating-Disk-Electrode (RDE) measurements

The electrochemical characterization was conducted in a three-electrode electrochemical cell. The cell consists of a Pt foil (counter electrode), an Ag wire quasireference electrode (~3.1 V vs Li$^+$/Li), and a glass carbon (GC) electrode (a working electrode) loaded with samples. This GC is fixed in a rotating disk electrode

(RDE, GC disk with radius of 2.80 mm). The electrolyte is 1 M LiTFSI in TEGDME with different concentrations of Co^{II}-salen. The electrolyte was saturated with high-purity O_2 or Ar (Air Product, purity 99.995%). ORR test in O_2 was conducted using O_2 saturated electrolyte and purging the liquid level with Ar to guarantee that the consumed O_2 for Li_2O_2 formation comes from the electrolyte. For the preparation of catalyst films, the MCNTs or MCNTs@MnO_2 (10 mg) was ultrasonically dispersed into 1000 μL of 950:50 v/v isopropyl alcohol/neutralized nafion solution (5 wt%, Sigma-Aldrich) to form a black ink. Then, 7.0 μL of the ink (containing 70 μg of carbon) was loaded onto the GC electrode and naturally dried for 10 h. The carbon loading was ~0.284 mg cm^{-2}. In linear sweep voltammetry (LSV) test, the disk electrode was scanned at a scanning rate of 2 mV s^{-1} with a rotating speed of 900 r min^{-1}.

Powder electrochemical impedance spectroscopy (PEIS) measurements

We create a simple method of PEIS to value intrinsic electron transport kinetics of sample powders. The PEIS device consists of an anode case (20 mm in diameter and 0.25 mm in thickness) and a stainless steel spacer (1.0 mm in thickness) of 2032-coin type. Powder samples (with fixed mass of 6 mg) were pressed (10 kPa cm^{-2}) in the interlayer of the anode case and the stainless steel spacer. The following step is the same as electrochemical impedance spectroscopy (EIS) test that was measured on an AC voltage of 5 mV amplitude in the frequency range from 100 kHz to 100 mHz. The nanocomposite showed a much smaller semicircle (1.26 kΩ) than MCNTs/MnO_2

mixture (3.70 kΩ). This result suggests that MCNTs@MnO_2 has a higher electron transport through the interface of MCNTs and MnO_2 than that of MCNTs/MnO_2 mixture. Notably, MCNTs@MnO_2 nanocomposite and MCNTs/MnO_2 mixture has same MnO_2 content (57%), which is confirmed later.

Apparent O_2 solubility caculation

According to the reaction of $2Li^+ + O_2 + 2e^- \leftrightarrow Li_2O_2$ and the formula of $C_{th} = 26800 \times n/M$, capacity of 1675.1 mAh is output by comsuming 1 g of O_2. In the above formula, n is transfer electron number, 2; M is molecular weight, 32 g mol^{-1}. The discharge capacity with and without 5 mM Co-salen at 10 mA g^{-1} is 0.0247 mAh and 0.0026 mAh, respectively, corresponding to 4.61×10^{-7} mol and 4.85×10^{-8} mol of O_2. In consideration of the electrolyte volume of 100 μL, we obtain the apparent O_2 solubility of 4.61 mM and 0.49 mM for 5 and 0 mM salen, respectively. In fact, the dissolved O_2 in the electrolyte could not be completely consumed, because of the existance of O_2 concentration gradient. Thus, the real value of O_2 solubility is higher than above apparent value.
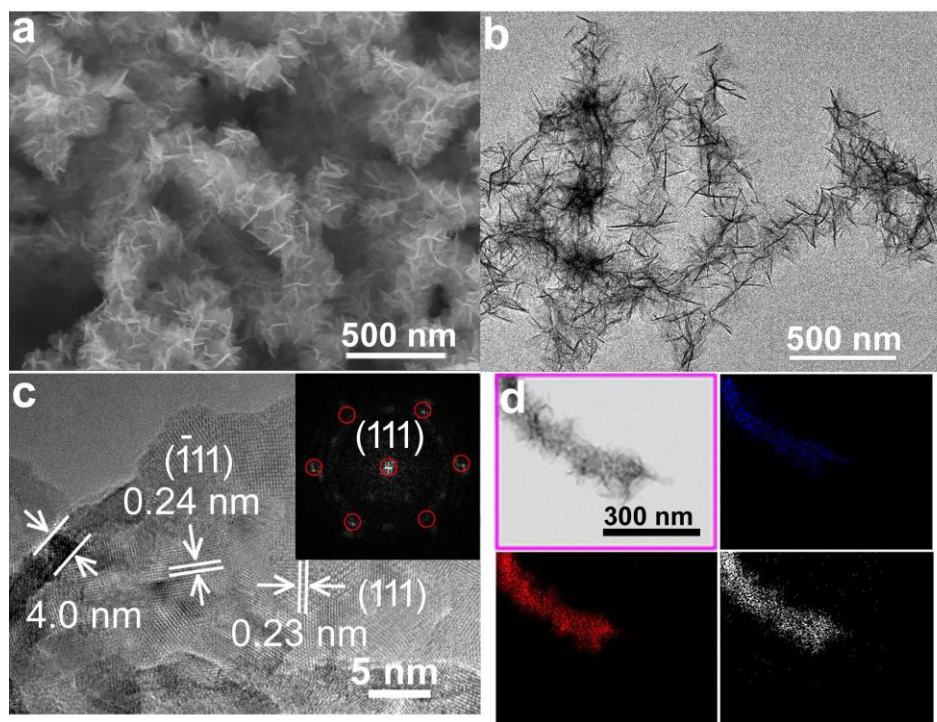
Figure S1. The morphology and crystal lattice of MCNTs@MnO$_2$-L. (a) SEM image, (b) TEM image, and (c) HRTEM images of MCNTs@MnO$_2$-L. (d) Energy-dispersive X-ray (EDX) mapping (of the C, Mn, and O elements) of MCNTs@MnO$_2$-L.

In comparison with coating time of 1.5 h, as the coating time went longer (3 h), we obtained the over coated composite (labeled as MCNTs@MnO$_2$-L), in which MnO$_2$ nanosheets wrapped outside and its diameter increased to ~230 nm. The EDX mappings of particular regions clearly show the core-shell structure of MCNTs@MnO$_2$-L consisting of inner MCNTs and outer MnO$_2$ layers.
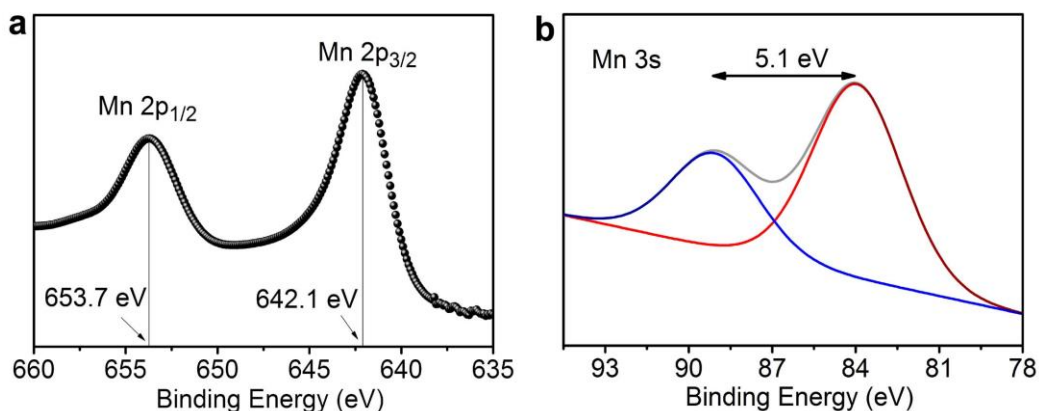
Figure S2. XPS survey of MCNTs@MnO$_2$: (a) Mn 2p, (b) Mn 3s.

We also applied surface elemental analysis by X-ray photoelectron spectroscopy (XPS) on MCNTs@MnO$_2$. The high-resolution Mn 2p core level spectra show that Mn 2p$_{3/2}$ (642.1 eV) and Mn 2p$_{1/2}$ (653.7 eV) show a spin energy separation of 11.6 eV, which is in agreement with the reported data for MnO$_2$.[1−4] The splitting width of the Mn 3s doublet peaks is 5.1 eV, indicating that its oxidation state is between 3.5−4.[5] This result is also consistent with soft X-ray spectroscope. The fact that Mn valence between 3.5−4 rather than 4 is probably caused by oxygen defects, which is good for ORR/OER catalysis.[6]
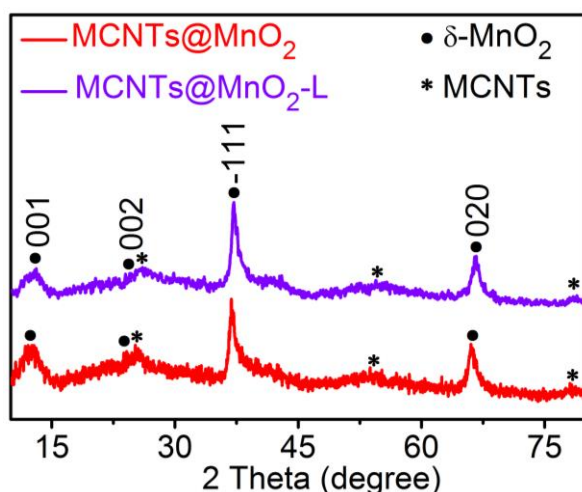
Figure S3. XRD of MCNTs@MnO$_2$ and MCNTs@MnO$_2$-L.

Soft X-ray absorption spectroscopies (SXAS) are used to reveal the valence bond transition during synthesis procedure of MCNTs@MnO$_2$ nanocomposite. At the carbon K-edge, we can obviously observe a significant increase in the peak absorption intensity around 289 eV as compared to MCNTs control, which is attributed to the C−O functional groups on MCNTs.[7] This suggested possible formation of C−O−Mn bonds in the composite materials. As the reaction time turns longer (MCNTs + KMnO$_4$ → CO$_2$↑ + MCNTs@MnO$_x$ + K$_2$CO$_3$), the peak intensity of C=C bond (~286 eV) decreases, because abundant C=C open along with more and more C-O-Mn (~289 eV) formation.[8,9] Besides, a lower adsorption intensity of the π* peak of ~286 eV (C−K edge) of the composites as compared to the MCNTs control is observed, suggesting possible electron transfer from Mn to MCNTs in the composite material.[10] The bond formations and charge transfer indicate the intimate couplings between MnO$_x$ coating layer and MCNTs. Based on the earlier reports of the O K-edge absorption spectra,[11,12] the first intense pre-edge peaks (530.4 eV and 533.0 eV) corresponds to the transition of O 1s electron to the hybridized state of Mn 3d and O 2p orbitals, whereas the broad higher energy peaks (around 545 eV) correspond to the transitions to hybridized states of O2p and Mn 4sp orbitals. Namely, peaks at 530.4 eV and 533.0 eV are from the electron jump of O1s to eg↑t2g↓ and eg↓of Mn3d orbits in MnOx. For the Mn ions in MCNTs@MnO$_2$ and MCNTs@MnO$_2$-L, the peaks at 640 to 645 eV and 654.5 eV are due to the respective electronic transitions from Mn 2p$_{3/2}$ and 2p$_{1/2}$ core level.[13] The peak intensity of Mn (IV, 642.0 eV and 644.4 eV) increases with reaction going, suggesting that the trace of Mn (II, 641.3 eV) and tiny of Mn (III, 643.0 eV) continuously transform to Mn (IV). According to the change of peak intensity in MCNTs@MnO$_2$ and MCNTs@MnO$_2$-L, proportion of Mn (IV) increase and proportion of Mn-ion with low valence state decreases, also indicating the transformation from Mn (II) and Mn (III) to Mn (IV). The data shown by SXAS suggest that a small amount of low-valence Mn-ion and large amount of Mn (IV) form at early stage of the synthesis reaction, and as reaction time prolongs, more and more C-O-Mn forms and the surviving low-valence Mn-ion continuously transform to Mn (IV).
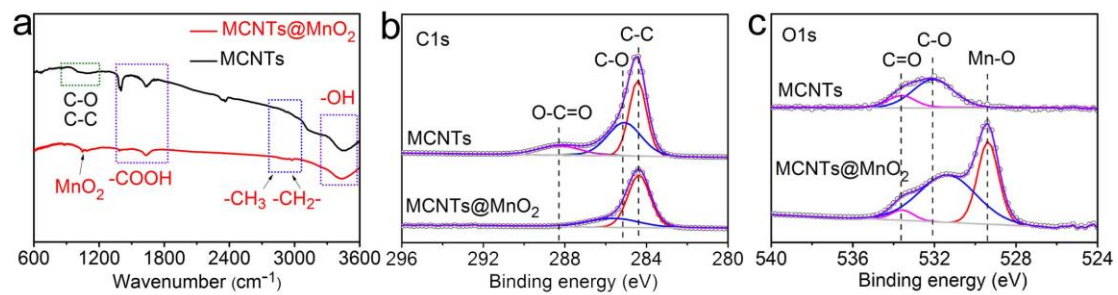
Figure S4. FT-IR and XPS of MCNTs and MCNTs@MnO$_2$ nanocomposite. (**a**) FT-IR of MCNTs and MCNTs@MnO$_2$. (b,c) XPS of (b) C1s and (c) O1s..
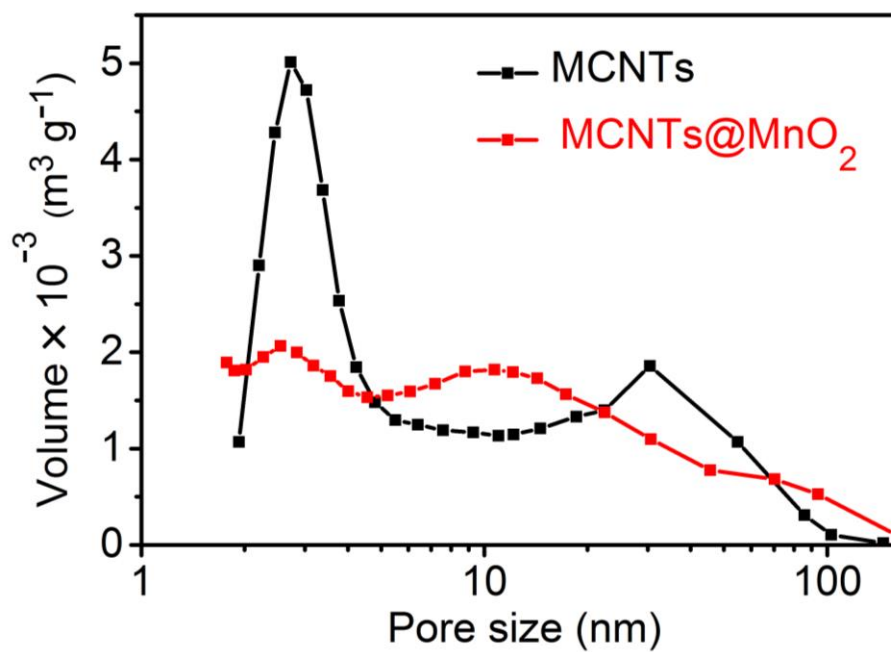
Figure S5. Pore distribution of MCNTs and MCNTs@MnO$_2$.
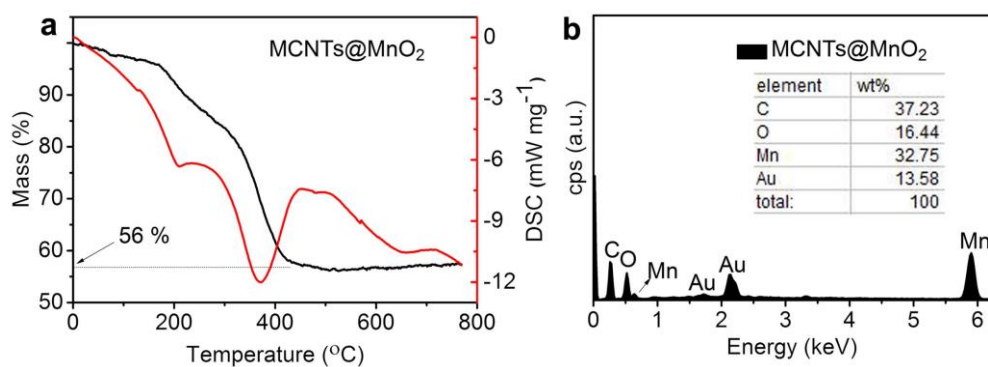
Figure S6. Thermal gravity analysis (TGA) curves and EDS spectra of MCNTs@MnO₂. (a) TGA curves below 780 °C measured with a heating rate of 5 °C min⁻¹ in air atmosphere. (b) EDS spectra. The content of C within the composite is ~43%.

Thermo-gravimetric analysis (TGA) of MWCNT@MnO₂ is shown above. Only ~4 wt% weight loss were observed until 173 °C, which result from the escape of adsorbed water and air. The fast weight losses until 450 °C mainly arise from the oxidation of MCNTs ($C + O_2 \rightarrow CO_2$), suggesting the mass content of carbon in the composite is about 43.0 wt%, which is in the agreement with large-scale EDX of the composite MCNTs@MnO₂.
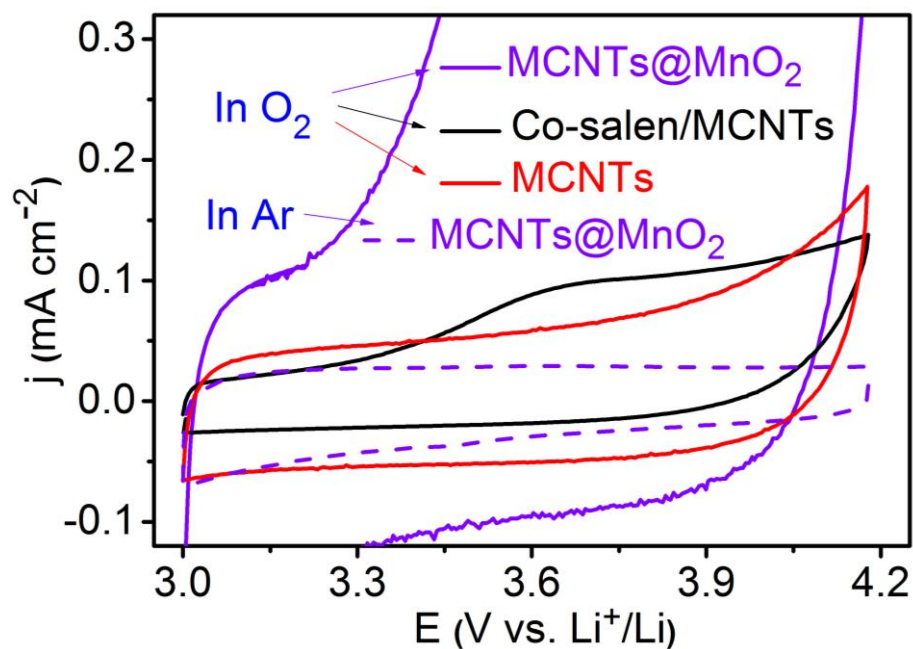
Figure S7. CV curves with speed of 1 mV s^{-1}. This figure combines amplifying curves in Figure 1h and CV curves of Co-salen/MCNTs. Co-salen/MCNTs stands for the LABs with 5 mM Co-salen in electrolyte and MCNT cathode.

Because the same amount of Li_2O_2 was deposited during discharge, the integrated area under the oxidation peaks for each electrode is identical in theory. In fact, the electrodes with Co-salen/MCNTs or MCNTs have poor catalytic activity towards Li_2O_2 decomposition and thus need higher voltage (>4.2 V) to oxidize Li_2O_2. So, the integrated areas under the oxidation peaks for each electrode between 3.0 and 4.2 V are not same. In order to eliminate the risk of electrolyte decomposition, the voltage window is limited below 4.2 V.

In addition, the weaker oxidation current and much higher onset potential of Co-salen/MCNTs than that of MCNTs@MnO₂, indicating poor catalytic activity of Co-salen/MCNTs towards Li_2O_2 decomposition.
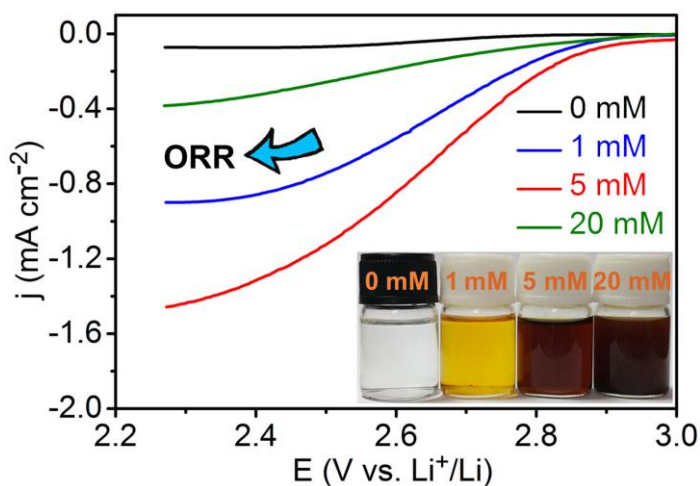
Figure S8. LSV curves under O_2 in electrolytes with different concentrations of Co^{II}-salen on MCNTs coated glassy carbon electrode at 900 r min^{-1} and 2 mV s^{-1}. The inset is the photographs of 1 M LiTFSI/TEGDME electrolytes with different concentrations of Co^{II}-salen from 0 mM to 1, 5, and 20 mM.

The concentration of Co^{II}-salen in 1 M LiTFSI/TEGDME electrolyte is adjusted from 0 mM to 1, 5, and 20 mM and the colors gradually vary from light-colored to dark in the inset graph. The linear sweep voltammetry (LSV) of these electrolytes on MCNTs coated glassy carbon electrode is shown above. In comparison with other three concentrations, the electrolyte with 5 mM Co^{II}-salen exhibits more positive ORR onset potential as well as higher catalytic current density. Therefore, the optimal concentration of Co^{II}-salen in the TEGDME based electrolyte is 5 mM.
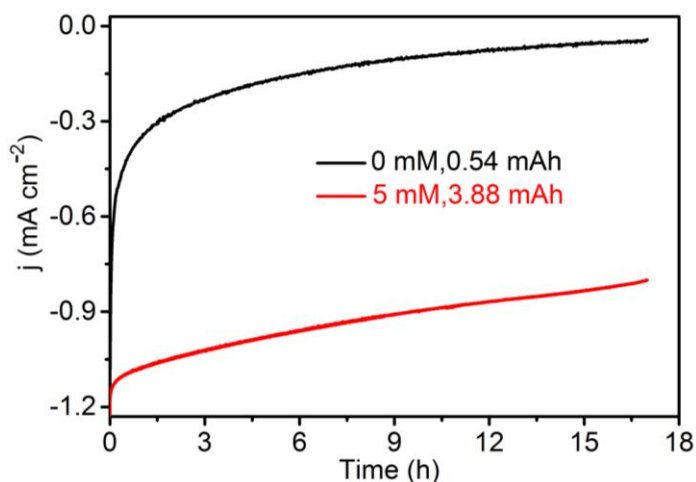
Figure S9. Current-time curves on MCNTs coated glassy carbon electrode at 400 r min^{-1}. The supporting electrolyte is 20 mL of 0 mM or 5 mM Co^{II}-salen/TEGDME electrolytes. The fixed potential is 2.5 V vs. Li$^+$/Li. It should be mentioned that electrolyte surface is purged by Ar after the electrolyte has been saturated by O$_2$. The integrated areas between current density and time are 3.88 mAh (5 mM Co-salen) and 0.54 mAh (0 mM Co-salen).

In order to invoid the limitation by pore volume and surface passivation of active sites of cathode, we add an experiment on the glass carbon electrode to study the effect of the Co-salen O$_2$-carrier on ORR in electrolytes of 0 mM or 5 mM Co^{II}-salen/TEGDME. By fixing the reduction potential of 2.5 V vs. Li$^+$/Li for 17 h, the oxygen reduction current of O$_2$-saturated electrolyte with Co-salen (0.80 mA cm^{-2}) is much larger than that without Co-salen (0.04 mA cm^{-2}). The capacities with and without Co-salen are 3.88 mAh and 0.54 mAh, respectively. At the potential of 2.5 V vs. Li$^+$/Li, O$_2$ and (Co-salen)$_2$-O$_2$ rather than Co-salen self could be reduced. So, above capacity only relates to O$_2$ consumption. Correspondingly, the apparent O$_2$-solubility without Co-salen is 0.51 mM, which is much smaller than that with Co-salen. Those data imply the much improved catalytic activity of Co^{II}-salen and its high reversible O$_2$ uptake capability. Notably, the value of apparent O$_2$-solubility without Co-salen is close to that calculated by battery discharge (0.49 mM) in Figure 2e.
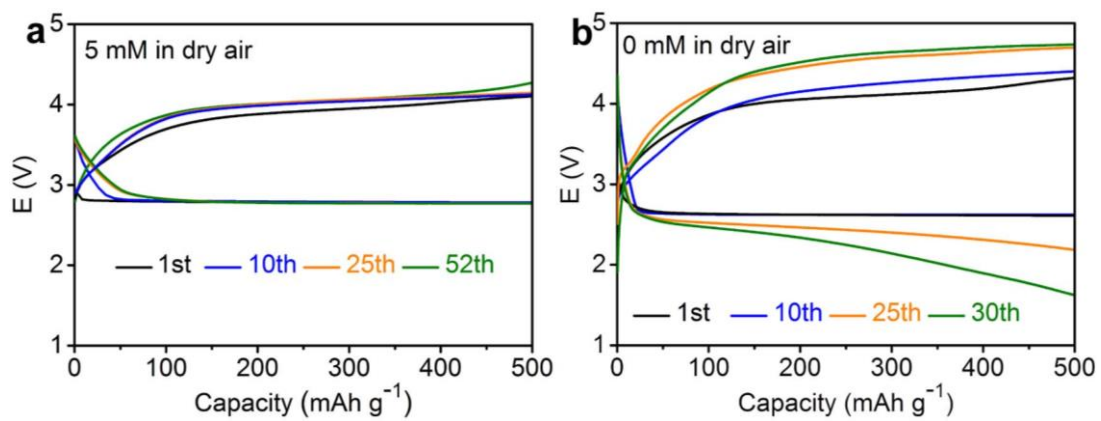
Figure S10. Discharge/charge profiles of LABs (a) with (b) without Co^{II}-salen in electrolytes in dry air. Rate, 250 mA g^{-1} (0.075 mA cm^{-2}). The capacity of 500 mAh g^{-1} corresponds to 0.15 mAh cm^{-2}.
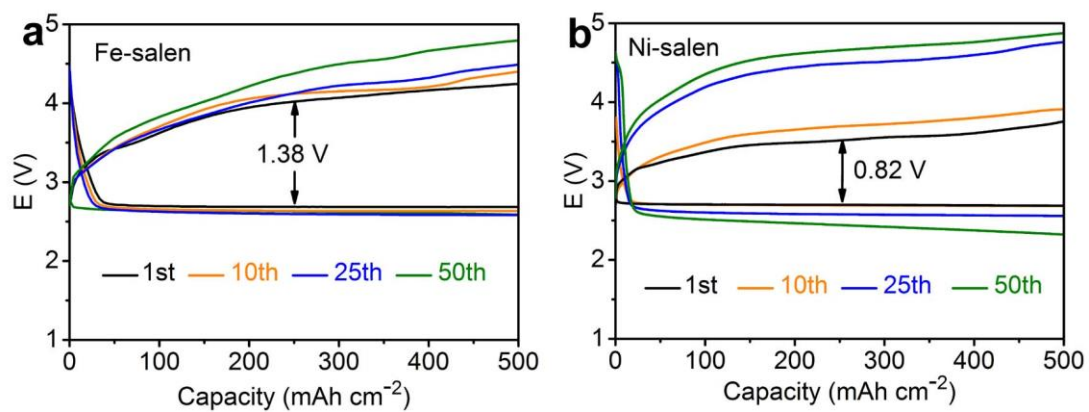
Figure S11. Electrochemical performance of LABs with (a) 5 mM Fe^{II}-salen and (b) 5 mM Ni^{II}-salen in electrolytes at 250 mA g^{-1} (0.075 mA cm^{-2}).
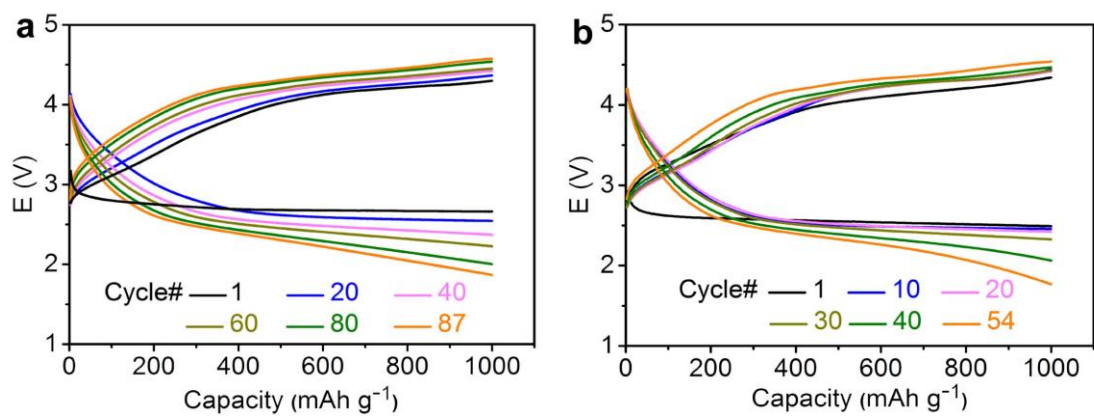
Figure S12. Charge/discharge cures of LABs with Co-salen/MCNTs@MnO$_2$ at different current densities with fixed capacity of 1000 mAh g^{-1} (0.30 mAh cm^{-2}): (a) 1 A g^{-1} (0.30 mA cm^{-2}), (b) 2 A g^{-1} (0.60 mA cm^{-2}).
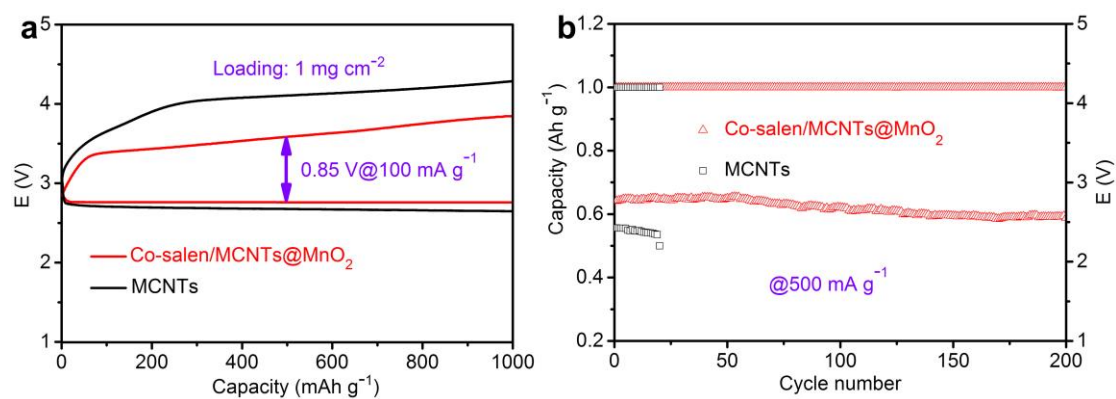
Figure S13. Battery performance in dry air with loading mass of 1 mg cm^{-2}. (a) Comparison of operating overpotentials at 100 mA g^{-1} (0.10 mA cm^{-2}). (b) Cyclability comparison with controlled capacity of 1000 mAh g^{-1} (1.0 mAh cm^{-2}) at 500 mA g^{-1} (0.50 mA cm^{-2}).
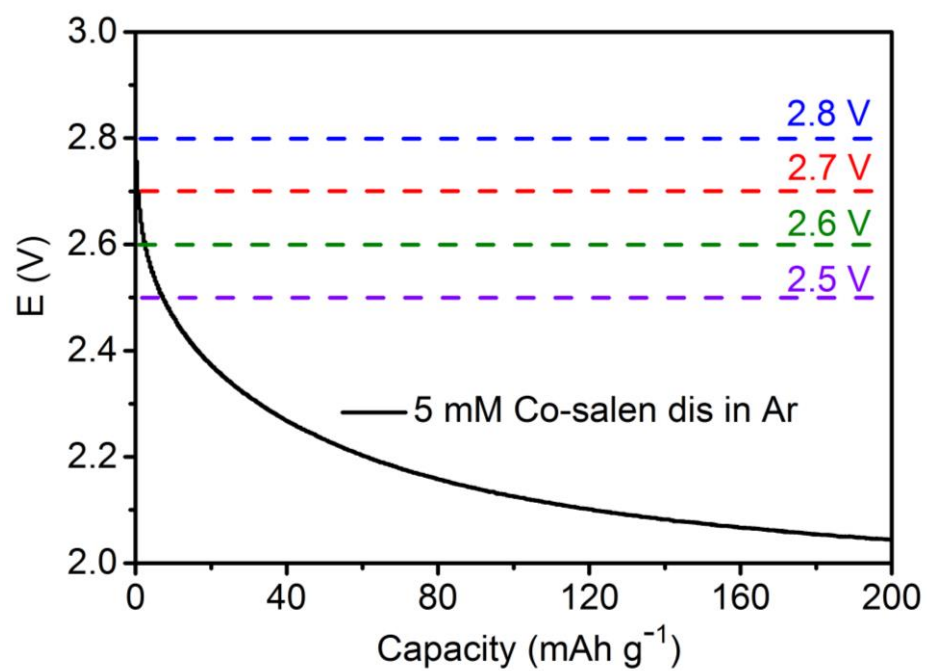
Figure S14. Discharge curve of LABs with Co-salen/MCNTs in Ar. Rate: 500 mA g^{-1} (0.15 mA cm^{-2}).
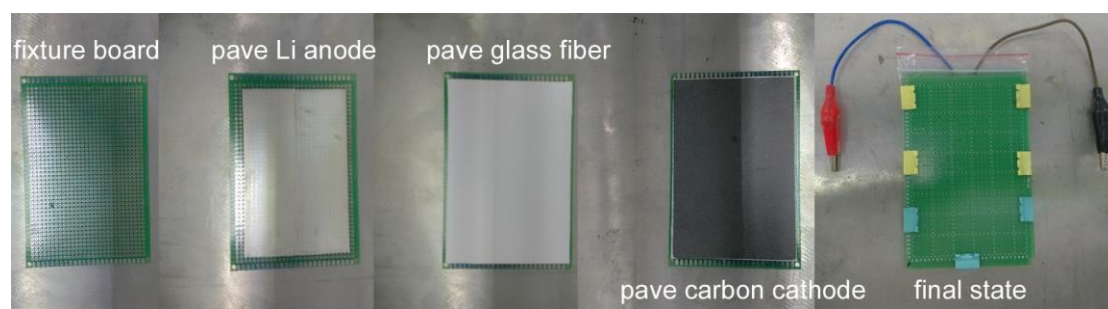
Figure S15. The assembly process of pouch-type LABs. Above glass fiber contains 5 mM Co-salen in 1 M LiTFSI/TEGDME.
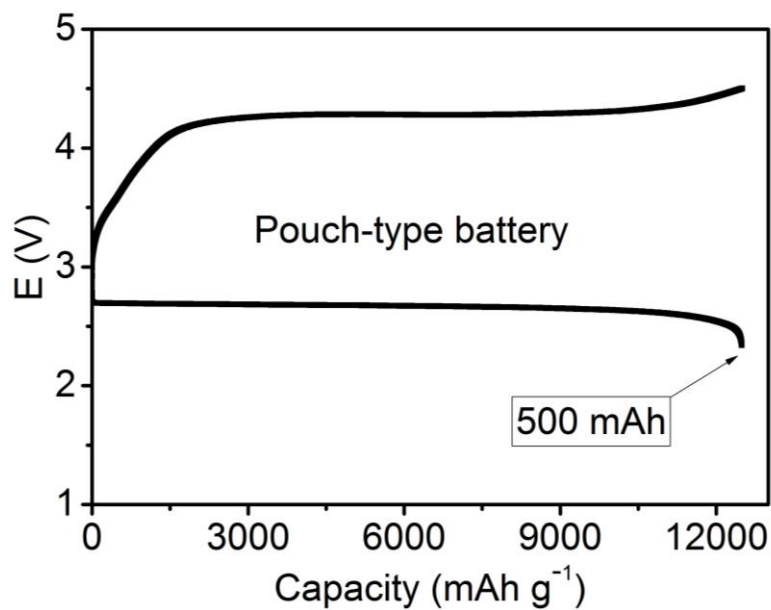
Figure S16. Discharge/charge profiles of pouch-type batteries.

Even though the charging overpotential of pouch-type LABs is higher than that of coin-type LABs, the charging process is also shown. The reversible discharge/charge capacity is 500 mAh, corresponding to 5.2 mAh cm^{-2}. In consideration of the total mass of the pouch-type battery is 4 g, the reversible capacity is 120 mAh g^{-1}. Optimizing the assembling technology is necessary to improve reversible capacity and reduce overpotentials.
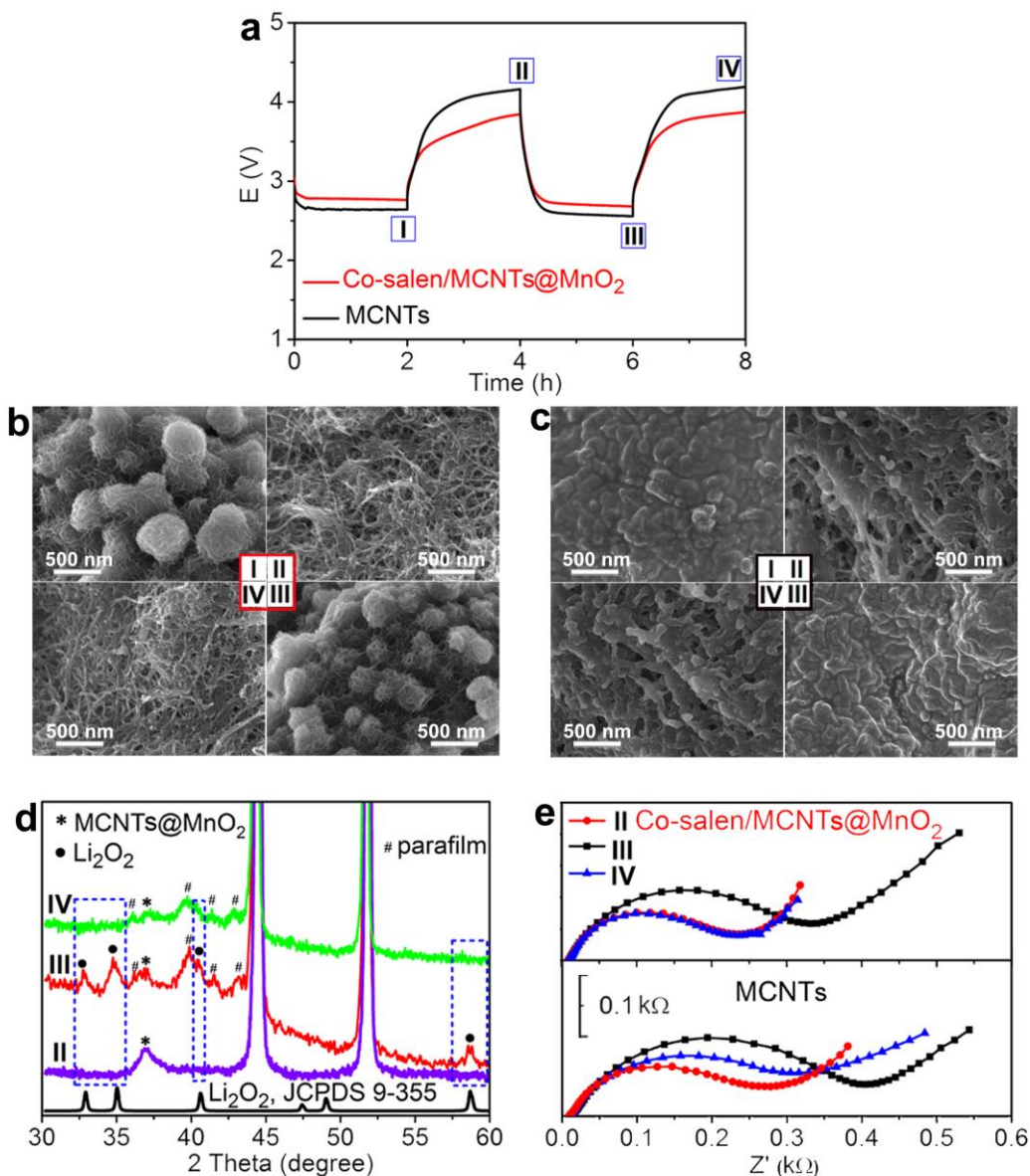
Figure S17. Process analysis of LABs with Co-salen/MCNTs@MnO$_2$ or only MCNTs. (a) Discharge and charge curves at 500 mA g^{-1} with and without catalysts. (b,c) SEM images of cathode at different states with different catalytic conditions, (b) Co-salen/MCNTs@MnO$_2$, (c) MCNTs. (d) XRD patterns. The parafilm is used to keep air off. (e) Impedance spectra of LABs with MCNTs and Co-salen/MCNTs@MnO$_2$.

In order to verify the superior rechargeability of LABs with two-catalyst system of Co-salen/MCNTs@MnO$_2$, the cathode was dismantled from the batteries and analyzed at 4 different discharge/charge states and the LABs with only MCNTs act as the counterpart (Figure S17a). After discharge to 1000 mAh g^{-1}, the MCNTs@MnO$_2$ cathode is covered by echinus-like product with diameter of ~500 nm (state I). After recharging, the uniformly stacked product vanishes (state II). With LABs cycling, echinus-like product repeatedly appear and disappear (state III and state IV) (Figure S17b), suggesting the high catalytic efficiency of Co-salen/MCNTs@MnO$_2$ system towards ORR and OER. On the contrary, the discharge product

of MCNT cathode is aggregated and residuals are still can be observed on MCNT surface after charging or recharging (Figure S17c), indicating the difficulty on decomposing discharge products. The morphology difference of discharge products also confirms that two-catalyst system of Co-salen/MCNTs@MnO_2 accelerates Li_2O_2 formation in electrolyte.

The discharged/charged cathodes of the LABs with Co^{II}-salen in the electrolyte and operated in dry air were analyzed by X-ray diffraction (XRD) (Figure S17d). The reversible formation and decomposition of Li_2O_2 in the discharging and charging processes can be monitored by its characteristic diffraction peaks in comparison with the standard Li_2O_2. This is in accordance with the discharge/charge profiles in Figure S17a. In electrochemical impedance spectroscopic analysis (EIS) of LABs with Co-salen/MCNTs@MnO_2, the charge-transfer resistance (R_{ct}) is increased from 230 to 330 Ω after the first discharge. While, R_{ct} is recovered to 232 Ω after charge. This indicates reversible generation and decomposition of Li_2O_2 at the cathode surface.[14] In comparison, the impedance of MCNT based LABs endured 245, 365, 320 Ω at pristine, discharged, and recharged states, respectively (Figure S17e). The unrecovered R_{ct} agreed well with the recharged cathode containing residuals in Figure S17c (state IV) due to insufficient OER ability.
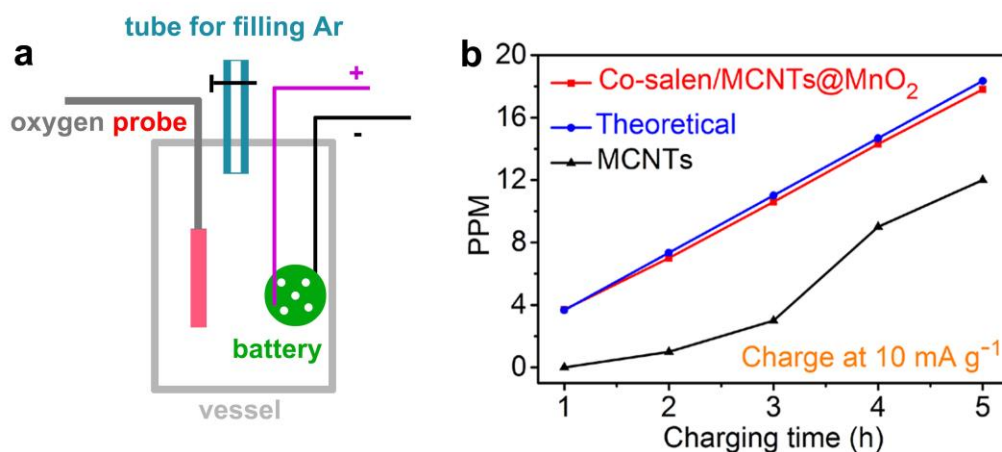
Figure S18. (a) Quantitative detection of O_2 during battery charging at 10 mA g^{-1}. (b) OER test of LABs with different catalytic conditions.

Quantitative detection of O_2 is carried out in a vessel with 500 mL of Ar. A discharged battery with or without 5 mM Co-salen and an O_2 probe (TAMASAKI, B-506, ± 0.01 ppm) are in the vessel. Quantitative detection of O_2 during battery charging is also carried out. The LABs with two-catalyst system of Co-salen/MCNTs@MnO$_2$ actually produce O_2, the amount of which is close to its theoretical value (3.56 ppm min^{-1}). This shows a much higher OER efficiency than that with only MCNTs.
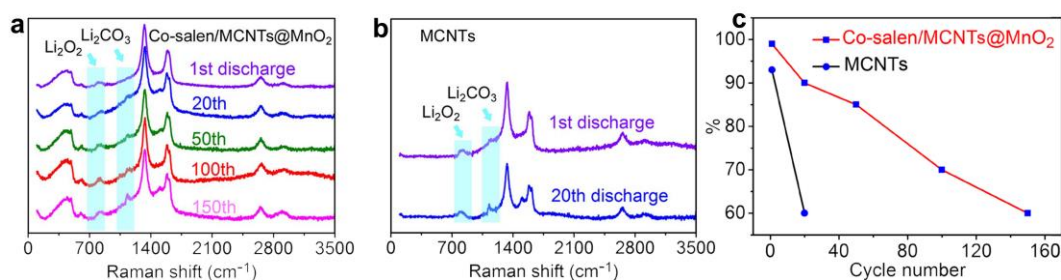
Figure S19. Chemical yields of LABs with different catalytic systems. (a,b) Raman spectra of cathodes in LABs with (a) Co-salen/MCNTs@MnO$_2$ and (b) MCNTs. (c) Mass percent of Li$_2$O$_2$ in discharge products of Li$_2$O$_2$ and Li$_2$CO$_3$.

The Raman (DXR 633 nm laser) indicates that the LABs with both MCNTs and two-catalyst system after the 1st discharge are dominated by Li$_2$O$_2$; while, after the 20th discharge, Raman offers solid evidence of serious side reactions on the MCNT cathode. In addition to Li$_2$O$_2$ (~790 cm^{-1}), the peaks at ~1100 cm^{-1} are assigned to Li$_2$CO$_3$. On the contrary, significantly weaker Raman peak of Li$_2$CO$_3$ is observed on the cathode with two-catalyst system after the 20th discharge. This may stem from the trace of CO$_2$ in dry air and the partial decomposition of the TEGDME-based electrolyte. We here use integral areas of Raman peaks to roughly calculate chemical yields of Li$_2$O$_2$. After the 1st discharge, the chemical yields are 99% and 93% in LABs with Co-salen/MCNTs@MnO$_2$ and only MCNTs, respectively. In sharp contrast, the chemical yields of Li$_2$O$_2$ in Co-salen/MCNTs@MnO$_2$ system is 60% after the 150th discharge, which is close to that of MCNT based LABs after 20 cycles. The obvious difference in chemical yield shows an effective suppression of side reactions due to the two-catalyst system of Co-salen/MCNTs@MnO$_2$ in comparison with MCNTs. How to circumvent or restrain the formation of Li$_2$CO$_3$ during long cycles in dry air (or ambient air with 300 to 400 ppm of CO$_2$) is currently a material and technology challenge.
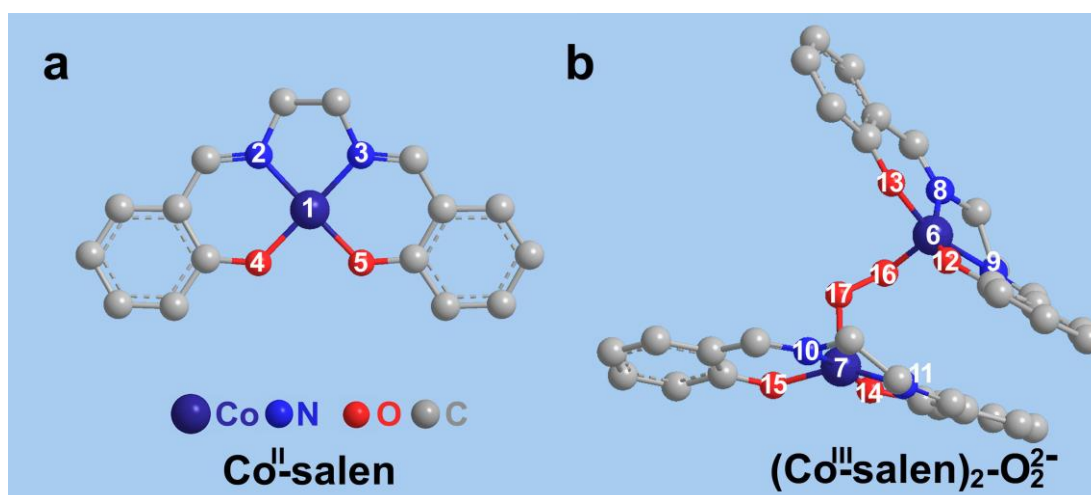
Scheme S1. DFT calculation on the molecular structure optimization of Co^{II}-salen and $(Co^{III}$-salen$)_2$-O_2^{2-}.

Table S1. Bond lengths (Å) of Co^{II}-salen and $(Co^{III}$-salen$)_2$-O_2^{2-}.

Co(1)-N(2)	1.86	Co(6)-N(9)	1.84	Co(7)-O(15)	1.86
Co(1)-N(3)	1.86	Co(6)-O(12)	1.88	Co(7)-O(17)	1.77
Co(1)-O(4)	1.84	Co(6)-O(13)	1.84	Co(7)-N(10)	1.84
Co(1)-O(5)	1.84	Co(6)-O(16)	1.79	Co(7)-N(11)	1.85
Co(6)-N(8)	1.86	Co(7)-O(14)	1.84	O(16)-O(17)	1.48

Table S2. Bond angles (º) of Co^{II}-salen and $(Co^{III}$-salen$)_2$-O_2^{2-}.

N(2)-Co(1)-N(3)	86.33	N(9)-Co(6)-O(12)	91.84	N(10)-Co(7)-O(14)	93.70
N(3)-Co(1)-O(5)	93.63	N(8)-Co(6)-O(13)	91.83	O(14)-Co(7)-O(15)	84.69
N(2)-Co(1)-O(4)	93.63	O(12)-Co(6)-O(13)	83.33	Co(6)-O(16)-O(17)	111.76
O(4)-Co(1)-O(5)	87.76	N(10)-Co(7)-N(11)	86.93	Co(7)-O(17)-O(16)	115.38
N(8)-Co(6)-N(9)	84.94	N(11)-Co(7)-O(15)	91.56		

The DFT calculations were implemented in Gaussian 09 Software.[15] All the structures were optimized at the B3LYP[16,17] level with the 6-31G (d) basis set, following by the frequency analysis to assure the real local minima. DFT calculations were performed to investigate the interaction between Co^{II}-salen and O_2. According to previous research,[18] the Co^{II}-salen tends to form 2:1 adducts with O_2, which is indicated by the electrons transferred number of ORR. The optimized geometry for the 2:1 complex is shown in Scheme 1b. The O-O bond length (d_{o-o}) of coordinated oxygen molecule is 1.48 Å, which is much longer than that of O_2 (1.21 Å), indicating the activation of O_2. Furthermore, the coordinated O-O bond length is close to that of O_2^{2-}(1.55 Å) in Li_2O_2 and Na_2O_2, confirming the formation of $[Co^{III}$---O_2^{2-}---$Co^{III}]$, which results in the excellent oxygen uptake capability of Co^{II}-salen. Thus, the activated O_2 can facilitate the following electrochemical reaction.

References

(1) Zhang, N.; Zhao, Q.; Han, X. P.; Yang, J. G.; Chen, J. *Nanoscale* **2014**, *6*, 2827−2832.

(2) Oh, S. H.; Black, R.; Pomerantseva, E.; Lee, J. H.; Nazar, L. F. *Nat. Chem.* **2012**, *4*, 1004–1010.

(3) Cheng, F. Y.; Chen, J. *Nat. Chem.* **2012**, *4*, 962–963.

(4) Hu, X. F.; Han, X. P.; Hu, Y. X.; Cheng, F. Y.; Chen, J. *Nanoscale* **2014**, *6*, 3522–3525.

(5) Toupin, M.; Brousse, T.; Bélanger, D. *Chem. Mater.* **2004**, *16*, 3184–3190.

(6) Cheng, F. Y.; Zhang, T. R.; Zhang, Y.; Du, J.; Han, X. P.; Chen, J. *Angew. Chem. Int. Ed.* **2013**, *52*, 1–5.

(7) Zhang, L.-S.; Liang, X.-Q.; Song, W.-G.; Wu, Z.-Y. *Phys. Chem. Chem. Phys.* **2010**, *12*, 12055−12059.

(8) Yoon, W. S.; Balasubramanian, M.; Yang, X. Q.; Fu, Z. G.; Fischer, D. A.; McBreen, J. *J. Electrochem. Soc.* **2004**, *151*, A246−A251.

(9) Zhou, J. G.; Hong, D.; Wang, J.; Hu, Y. F.; Xie, X. H.; Fang, H. T. *Phys. Chem. Chem. Phys.* **2014**, *16*, 13838−13842.

(10) Zhou, J. G.; Fang, H. T.; Hu, Y. F.; Sham, T. K.; Wu, C. X.; Liu, M.; Li, F. J. Phys. Chem. C **2009**, *113*, 10747−10750.

(11) Montoro, L. A.; Abbate, M.; Rosolen, J. M. *Electrochem. Solid-State Lett.* **2000**, *3*, 410−412.

(12) Uchimoto, Y.; Sawada, H.; Yao, T. *J. Power Sources* **2001**, *97*, 326−327.

(13) Yoon, W. S.; Chung, K. Y.; Nam, K. W.; Kim, K. B. *J. Power Sources* **2006**, *163*, 207−210.

(14) Gerbig, O.; Merkle, R.; Maier, J. *Adv. Mater.* **2013**, *25*, 3129–3133.

(15) Frisch, M. J.; Trucks, G. W.; Schlegel, H. B.; Scuseria, G. E.; Robb, M. A.; Cheeseman, J. R.; Scalmani, G.; Barone, V.; Mennucci, B.; Petersson, G. A.; Nakatsuji, H.; Caricato, M.; Li, X.; Hratchian, H. P.; Izmaylov, A. F.; Bloino, J.; Zheng, G.; Sonnenberg, J. L.; Hada, M.; Ehara, M.; Toyota, K.; Fukuda, R.; Hasegawa, J.; Ishida, M.; Nakajima, T.; Honda, Y.; Kitao, O.; Nakai, H.; Vreven, T.; Montgomery, J. A.; Jr., Peralta, J. E.; Ogliaro, F.; Bearpark, M.; Heyd, J. J.; Brothers, E.; Kudin, K. N.; Staroverov, V. N.; Kobayashi, R.; Normand, J.; Raghavachari, K.; Rendell, A.; Burant, J. C.; Iyengar, S. S.; Tomasi, J.; Cossi, M.; Rega, N.; Millam, J. M.; Klene, M.; Knox, J. E.; Cross, J. B.; Bakken, V.; Adamo, C.; Jaramillo, J.; Gomperts, R.; Stratmann, R. E.; Yazyev, O.; Austin, A. J.; Cammi, R.; Pomelli, C.; Ochterski, J. W.; Martin, R. L.; Morokuma, K.; Zakrzewski, V. G.; Voth, G. A.; Salvador, P.; Dannenberg, J. J.; Dapprich, S.; Daniels, A. D.; Farkas, O.; Foresman, J. B.; Ortiz, J. V.; Cioslowski, J.; Fox, D. J. Gaussian, Inc., Wallingford CT, **2009**.

(16) Becke, A. D. *J. Chem. Phys.* **1988**, *88*, 1053–1062.

(17) Lee, C.; Yang, W.; Parr, R. G. *Phys. Rev. B* **1988**, *37*, 785–789.

(18) Jones, R. D.; David, A. S.; Fred, B. *Chem. Rev.* **1979**, *79*, 139–179.